Table 2.6

Comparison of Oil Properties and Run Conditions for Continuous
Multiple Contact Experiments for Maljamar and Rock Creek Crude Oils

	Maljamar Separator Oil	Rock Creek Separator Oil	Rock Creek Separator Oil with selected aromatics
Aromatic Content (wt. %)	8	<2	14.8
Molecular Weight	200	190	174
Density (gm/cm^3)	0.832	0.797	0.813
Temperature (°F)	90	75	75
Pressure (psia)	1200	1300	1300

Table 2.7

Composition of Mixture of Aromatic
Hydrocarbons Added to Rock Creek Crude Oil

Component	Wt. %	Mole %
Toluene	30.98	40.24
1,2,4-Trimethylbenzene (TMB)	27.13	27.24
2-Methylnaphthalene (2MN)	23.85	19.51
Phenanthrene	18.03	13.01

Calculated Molecular Weight = 119.02

Table 2.8

Composition of Rock Creek Crude Oil
Mixed with Selected Aromatic Hydrocarbons

Component	Wt. %	Mole %
Rock Creek	85.21	78.30
Aromatics	14.79	21.70

Calculated Molecular Weight = 174.6

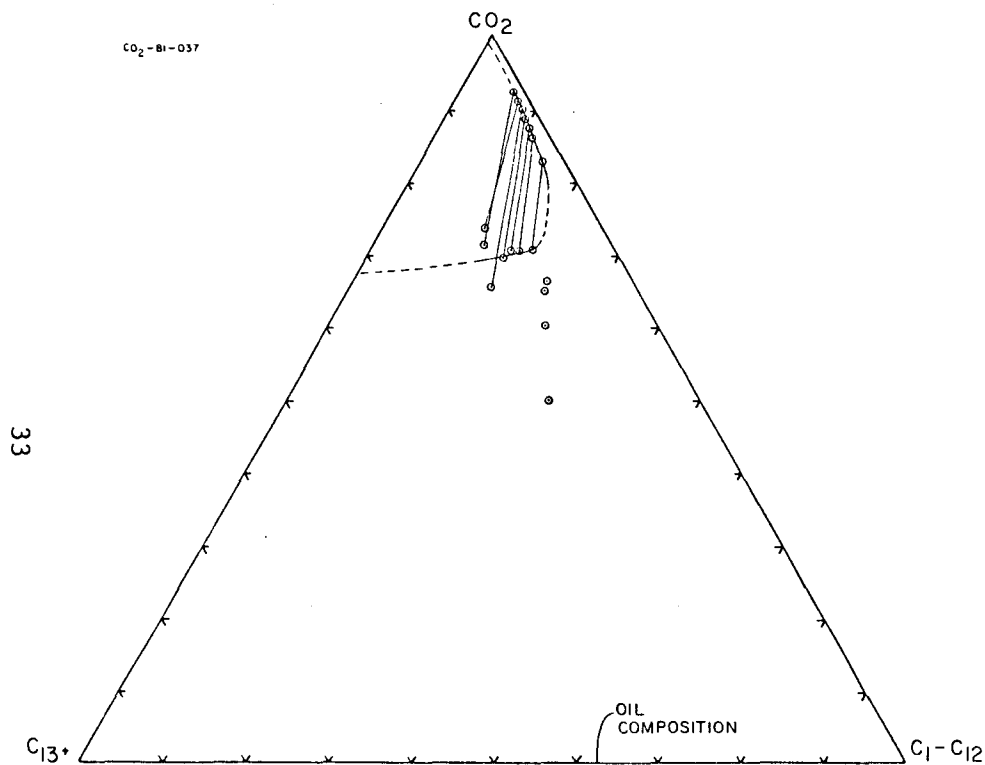Measured Molecular Weight = 173.5

Fig. 2.19   Pseudo-ternary representation of phase compositions of mixtures of CO_2 with Rock Creek oil containing added aromatic components at 1300 psia and 75°F.
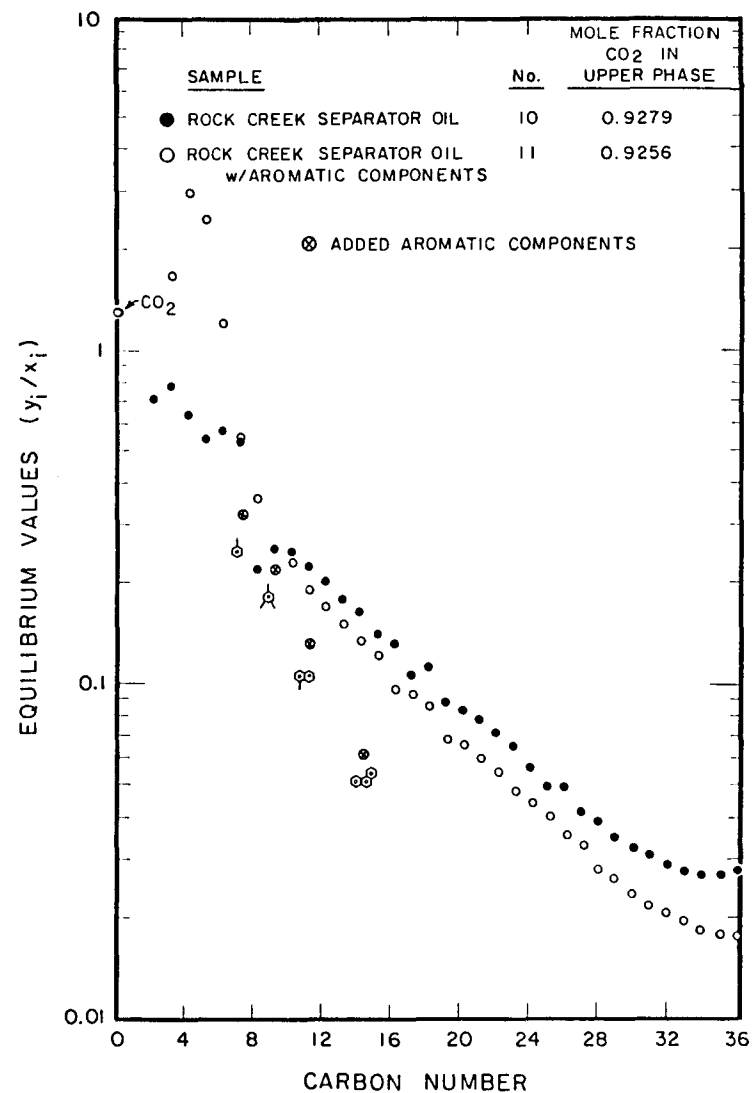

Fig. 2.20   Comparison of partition coefficients for Rock Creek oil and Rock Creek oil with aromatics added. Also shown are estimated K-values for the aromatic components added to the oil.

Fig. 2.20 compares equilibrium ratios as a function of carbon number for samples obtained in the runs with and without aromatics added containing about the same amount of CO_2. Comparison of the equilibrium ratio data was complicated somewhat by two factors. First, the aromatics added to the crude oil eluted later than the paraffin with the same carbon number. For example, the toluene eluted with C_8 alkanes, trimethylbenzene with C_{10} alkanes, 2-methylnaphthalene with C_{13} and phenanthrene with C_{18}. Second, the on-line chromatographic analysis of the produced vapor was stopped after the elution of the C_7 hydrocarbons in the run without aromatics. In the subsequent run with aromatics present, the vapor analysis was extended to make sure that any toluene present in the vapor was detected. Thus, the vapor composition data obtained in the two runs were not strictly comparable. Some distortion of the equilibrium ratio for C_8 is evident in the run for Rock Creek oil alone, for instance. Even though the amounts of C_8 present in the vapor were small, probably around one percent, the vapor volumes were large enough that some error in the C_8 K-value is apparent. To correct approximately for the measurement error and to estimate K-values for the aromatics, the following procedure was used:

(1) The amount of C_8 not detected in the run without aromatics was estimated from a material balance based on the amount and composition of aromatics added and an analysis of aromatic-crude oil mixtures.

(2) Hydrocarbons in the lower phase were assumed to have the same ratio of aromatics to crude oil hydrocarbons as in the uncontacted oil.

(3) K-values from the run without aromatics were used to estimate the amount of hydrocarbons from the oil present in the upper phase.

(4) The remaining hydrocarbons at the elution carbon number of the aromatics were assumed to be the aromatics that partitioned into the upper phase.

Typical results of K-values for the aromatic components are also shown in Fig. 2.20. They are plotted against the number of carbon atoms in the molecules rather than when they eluted during the analyses. While the toluene and trimethylbenzene showed K-values comparable to those of the hydrocarbons from the oil, the molecules containing two and three condensed rings were much less soluble in the CO_2-rich phase. While the K-values of the lightest hydrocarbons (C_3-C_6) appeared to be significantly higher when aromatics were present, the amounts of those hydrocarbons present were small enough that some of the difference could be scatter. For the hydrocarbons C_{10} and heavier, there was no evidence of an effect of the presence of aromatics.

Fig. 2.21 reports one additional piece of evidence on the effect of adding aromatics on extraction of hydrocarbons from the oil. The weight fraction liquid collected in the separator vials downstream of the back pressure regulators for the Rock Creek separator oil and Rock Creek separator oil with aromatics is plotted against a dimensionless time scale (Orr & Silva
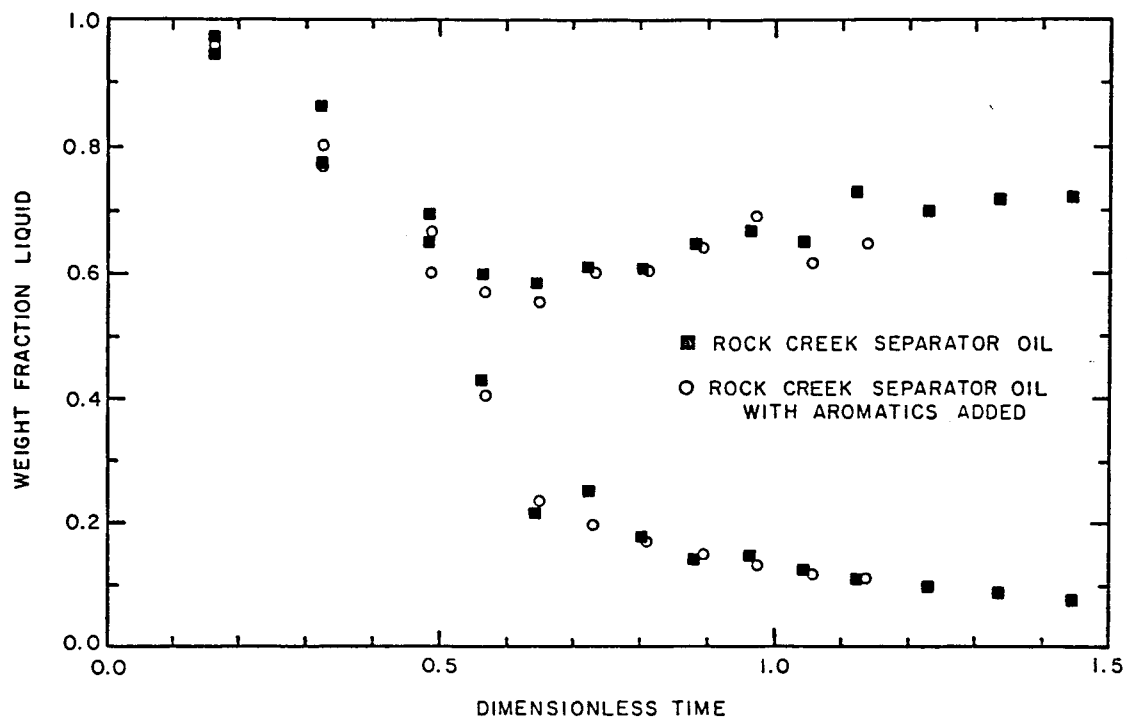
34

Fig. 2.21   Comparison of extraction of hydrocarbons by dense CO$_2$ for Rock Creek crude oil and Rock Creek oil with added aromatic components.
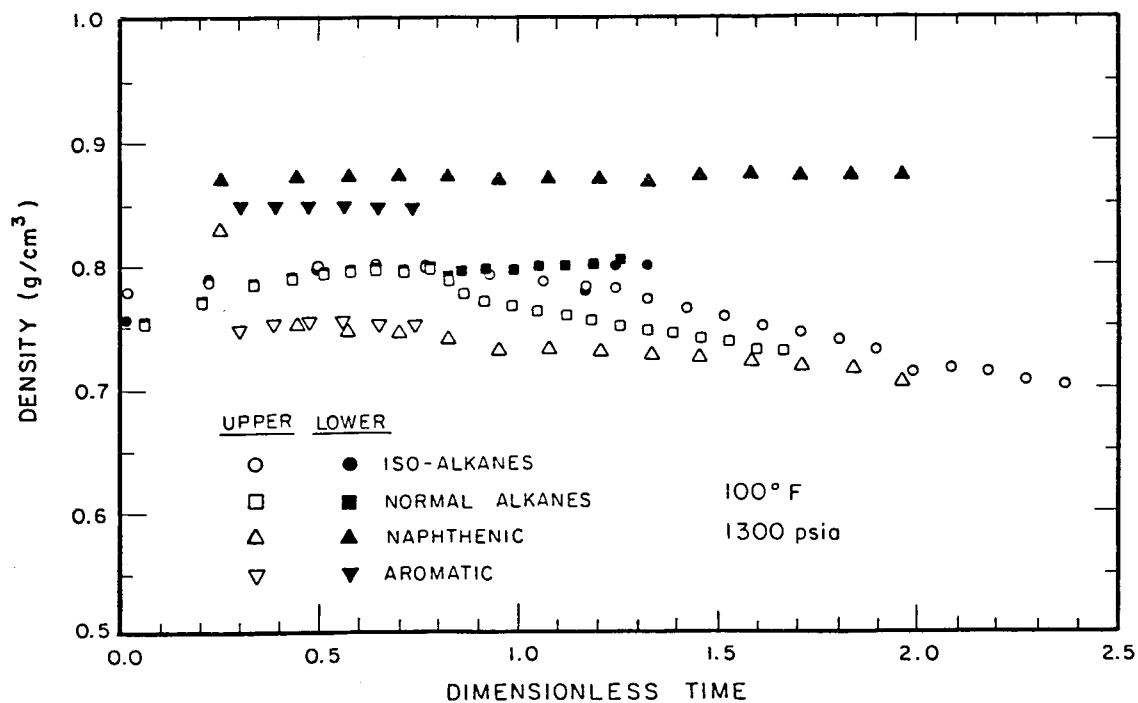

Fig. 2.22   Measured densities for CO$_2$-synthetic oil mixtures.

1983). As the experiment proceeded and CO_2 was added to the system, the weight fraction liquid declined until the overall composition reached the two-phase region. The weight fraction liquid for both systems was identical in the two-phase region indicating that the addition of aromatics to a paraffinic oil did not change the total amount of hydrocarbons extracted into the upper phase by carbon dioxide.

CO_2-Synthetic Oil Systems

The experimental results presented so far do not give a definitive answer concerning the effect of aromatics on CO_2-crude oil displacement behavior. It is not clear, for instance, whether the differences observed in the phase diagrams shown in Figs. 2.17 and 2.19 are the result of the addition of aromatics or the result of adding hydrocarbons of low molecular weight. Therefore, additional experiments were conducted on four synthetic oils to delineate the effects of oil composition and specifically the effects of hydrocarbon type on phase behavior. Table 2.9 lists the compositions and calculated molecular weights of the synthetic oils. Each oil contained similar amounts of light and intermediate components. In all of the oils, squalane, a branched paraffin (C_{30}), was the heavy component. All four studies were conducted at 100°F and 1300 psia. Phase density data, shown in Fig. 2.22, indicated that liquid-liquid phase behavior was observed.

Fig. 2.23 shows pseudo-ternary representations of the phase behavior of each synthetic oil with CO_2. Also shown for comparison is the phase diagram for Maljamar crude oil with CO_2. The crude oil system was studied at slightly different conditions, 90°F and 1200 psia. At those conditions CO_2 had a density of 0.660 g/cm^3 compared to 0.625 g/cm^3 for the synthetic oils. Results of static equilibrium PVT experiments (Orr, Yu & Lien 1981) and continuous multiple contact experiments (Orr, Silva & Lien 1983) suggest that the difference in conditions between the synthetic and crude oil systems probably had only a small effect on component partitioning. Comparison of the results indicates that the solubility of CO_2 was highest in the iso-alkane mixture, lower in the normal alkanes, lower still in the crude oil, and lowest in the naphthenic and aromatic mixtures. The sizes of the two-phase regions follow the same sequence.

Also shown in Fig. 2.23 are estimated positions of the tie lines tangent to the binodal curve at the plait point. The positions of the plait points were estimated by projecting the locus of midpoints of measured tie lines to the binodal curve obtained by extrapolating the upper and lower phase composition curves. The position of the critical tie line marks the boundary between oil compositions which will develop miscibility and those which will not. It has been shown (Hutchinson & Braun 1961; Helfferich 1981) for one-dimensional flow, in the absence of dispersion or other non-local mixing, that oils with compositions lying outside the region of tie line extensions are miscibly displaced, while those lying inside it are not. The size of the region of tie line extensions is determined by the slope of the critical tie line and the size of a two-phase region, as is illustrated in Fig. 2.24. Generally, the size of a two-phase region is reduced by an increase in pressure, and tie line slopes may also change. According to this simple

Table 2.9   Compositions and Molecular Weights
of Four Synthetic Oils

a.   Normal Alkanes

Component	Wt. %	Mole %
nC_5	7.00	17.84
nC_{10}	38.52	49.62
nC_{16}	23.73	19.21
C_{30}	30.74	13.33

Molecular Weight = 175.0

b.   Branched Alkanes

Component	Wt. %	Mole %
iC_5	6.07	15.84
iC_{10}	37.90	50.03
iC_{16}	23.99	19.90
C_{30}	32.03	14.23

Molecular Weight = 187.8

c.   Naphthenes

Component	Wt. %	Mole %
cyclopentane	9.10	21.66
decalin	37.65	45.46
perhydrofluorene	22.66	21.22
squalane	30.59	12.08

Molecular Weight = 167.0

d.   Aromatics

Component	Wt. %	Mole %
benzene	8.58	19.03
butylbenzene	39.53	51.05
phenyldecane	22.55	17.90
squalane	29.36	12.03

Molecular Weight = 173.4
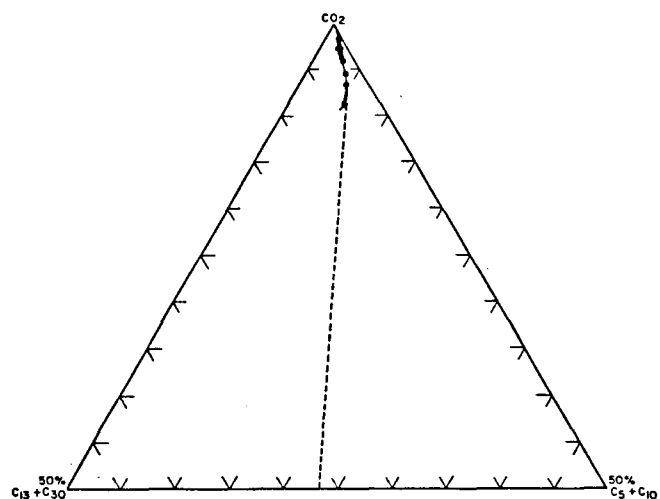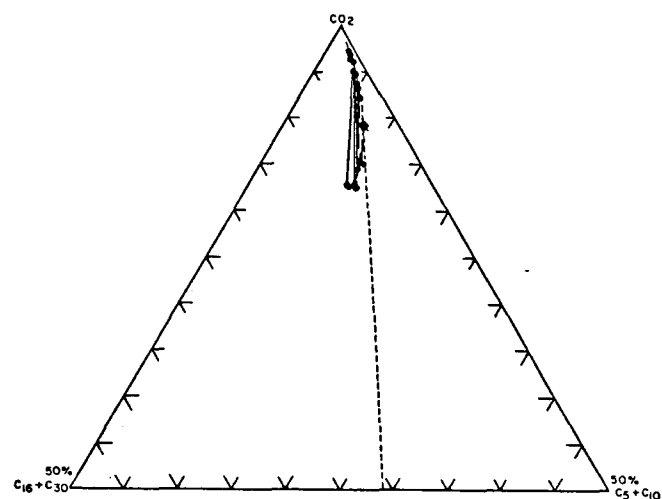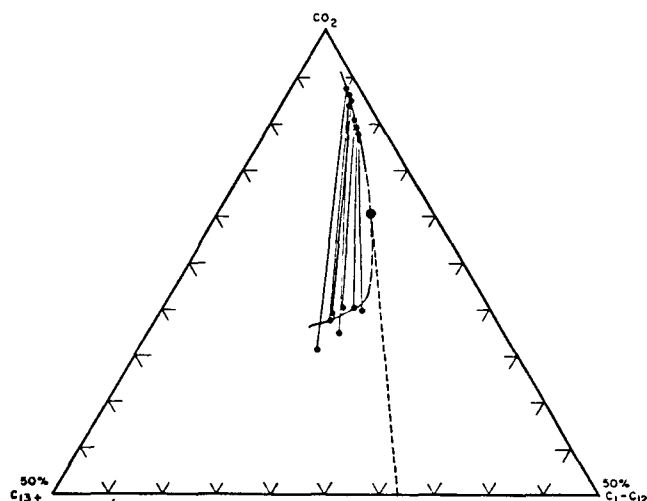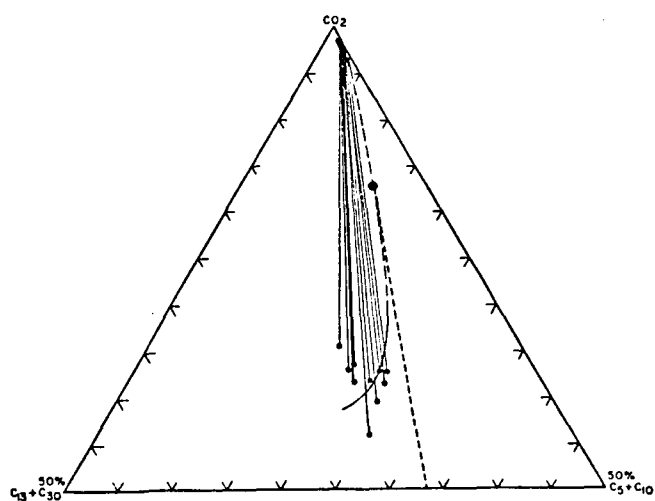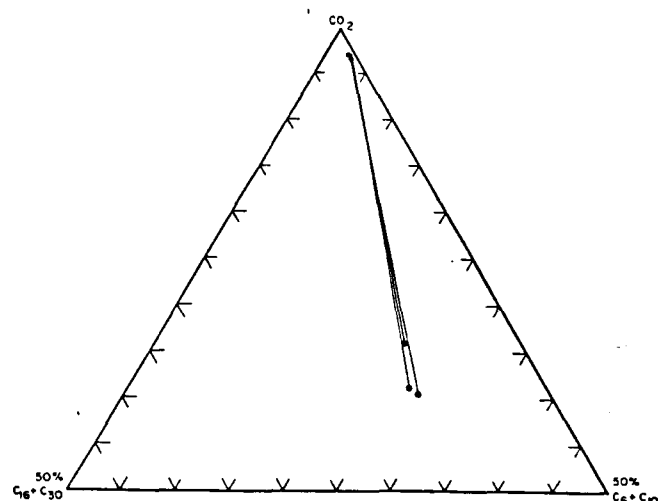
Fig. 2.23   Pseudo-ternary representations of phase compositions of CO_2-hydrocarbon mixtures.
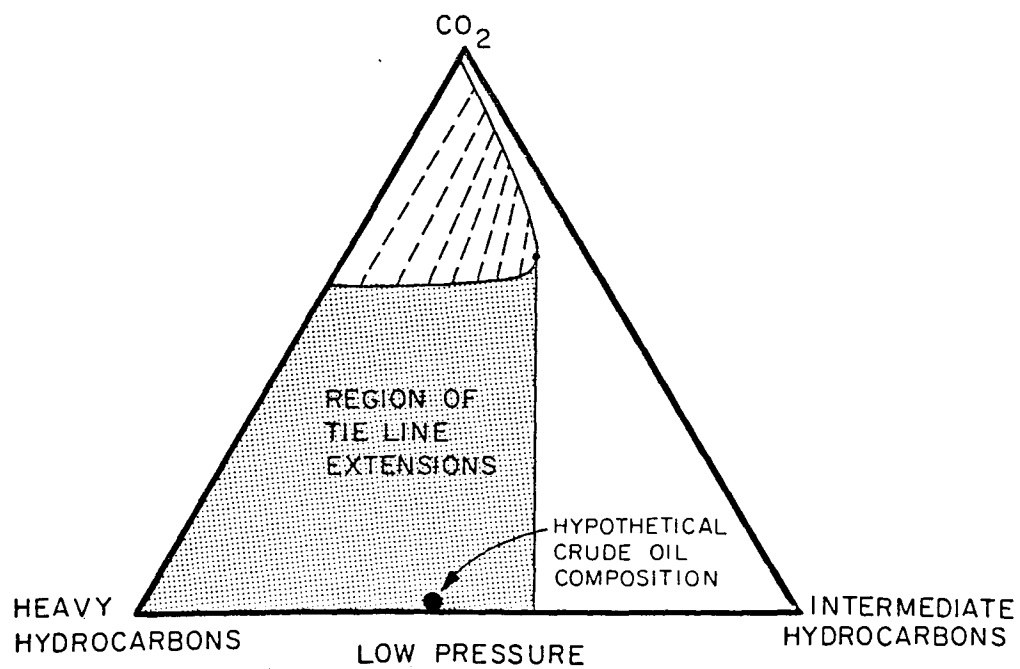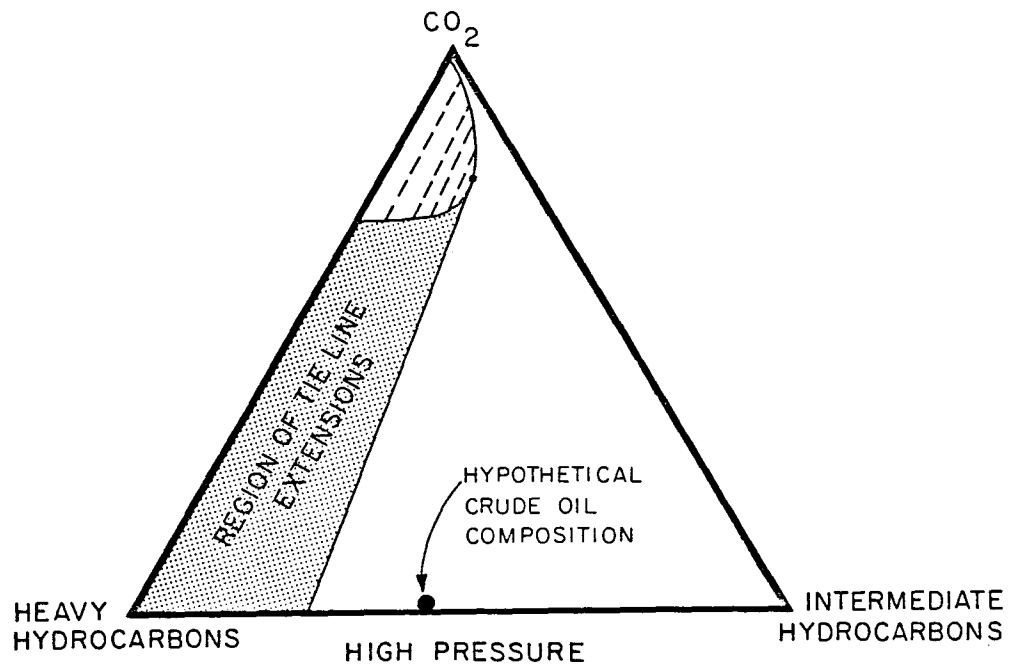
38

Fig. 2.24   Effect of pressure on the size of the region of tie line extensions.

qualitative argument, the MMP for a given oil is that at which the critical tie line is displaced so that the oil composition leaves the region of tie line extensions.

The results shown in Fig. 2.23 suggest, therefore, that the four synthetic oils studied here would have quite different MMPs. The small two-phase region and favorable tie line slopes of the branched alkanes produced a significantly smaller region of tie line extensions than those observed for the n-alkanes, naphthenes or aromatics. For instance, an oil containing 50 mol % C_5 + C_{10} would be multicontact miscible in the branched alkane system, but higher pressures would be required for the other oils. Fig. 2.25 reports equilibrium ratios for samples from the four CO_2-synthetic oil systems and the CO_2-Maljamar crude oil system. The samples selected for comparison contained approximately the same amount of CO_2 in the upper phase. Hydrocarbons in the branched paraffin mixture partitioned most strongly into the upper phase, followed by the straight chain alkanes, the aromatics, and the naphthenes. The crude oil ratios fall generally between the normal alkanes and naphthenes.

The relationship between equilibrium ratios and critical tie line behavior, as well as the rationale for comparing upper phases containing the same amount of CO_2, can be seen in Fig. 2.26. There are at least three ways that changing the molecular type of the hydrocarbon mixture can alter the phase diagram for the resulting mixtures with CO_2. The equilibrium distribution of components between phases may change (Fig. 2.26a), the solubility of CO_2 in the hydrocarbon may increase or decrease (Fig. 2.26b), or the amount of hydrocarbons extracted into the CO_2-rich phase may change. In practice, of course, the changes probably all occur to some extent when molecular types are changed. In Fig. 2.26, however, the qualitative effects of each type of change in phase behavior in ternary systems are examined individually while other features of the phase diagram are unchanged.

Case 1 shows the effect of changing tie line slope with the size of the two-phase region held constant. Because mixtures containing the same amount of CO_2 are compared, the upper phase compositions are identical. Equilibrium ratios are different for the two cases, though, because the lower phase compositions are different. Thus, mixtures which lie on tie lines a and b produce the same upper phases, but different lower phases. In mixtures on tie line b, component 2 partitions more strongly into the upper phase than it does for mixtures on tie line a, a fact that is reflected in the higher K-value of component 2 and lower K-value of component 3. Extrapolation of the tie lines to find the critical tie line (the tie line tangent to the binodal curve at the plait point) based on the assumption that all the tie lines meet at a point (Orr 1980) indicates that the stronger preferential extraction of tie line b translates into a smaller, more favorable, region of tie line extensions. For a given oil composition, then, the MMP would be lower for Case 1b than for Case 1a.

Similar reasoning can be applied to Case 2 and Case 3 where the tie line slopes are constant. Case 2 shows how increasing the solubility of CO_2 in the oil-rich phase raises the lower portion of the binodal curve and shifts the plait point to higher CO_2 concentrations to give a slightly more favorable
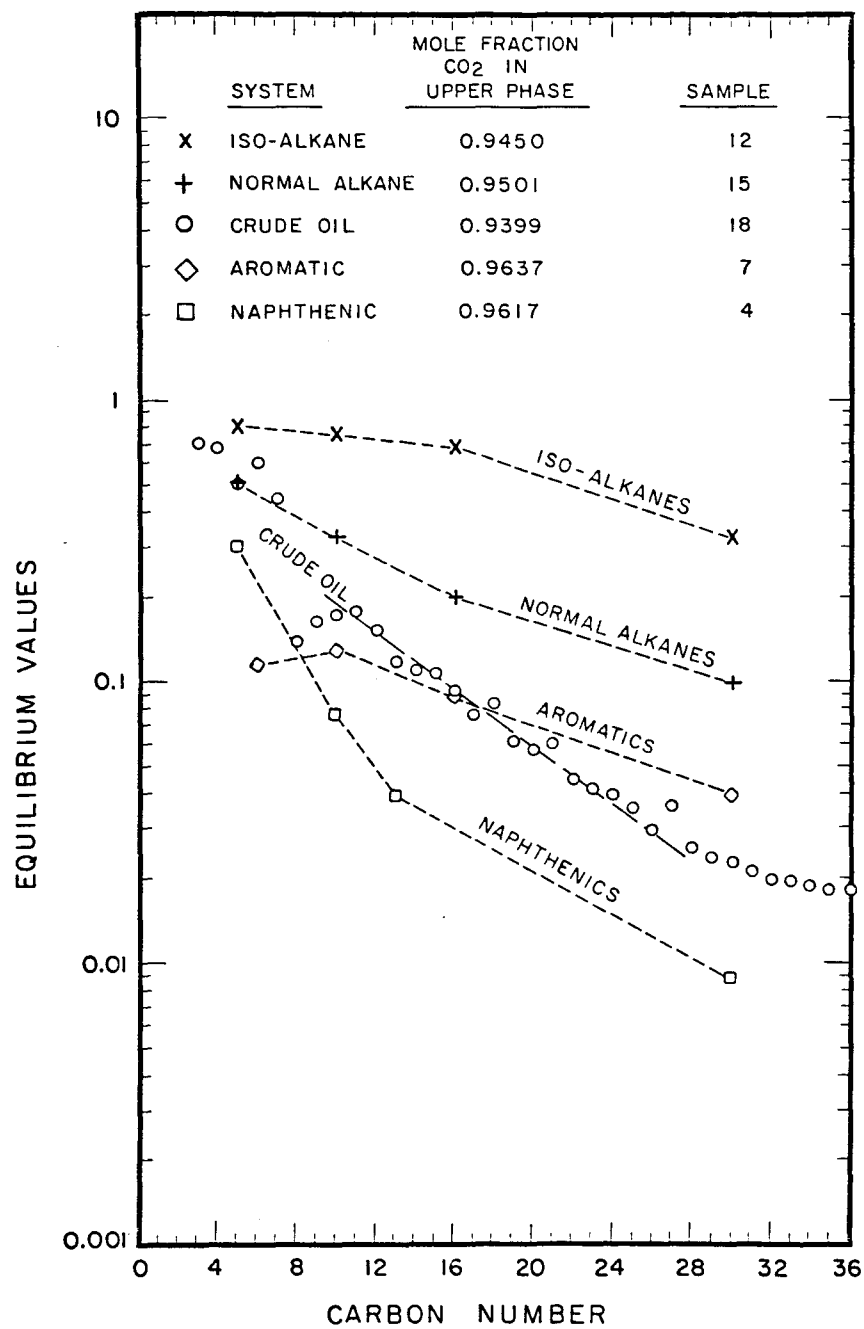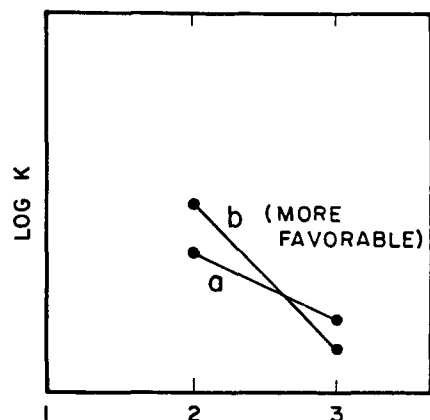
Fig. 2.25   Partition coefficients in CO_2-synthetic oil mixtures.
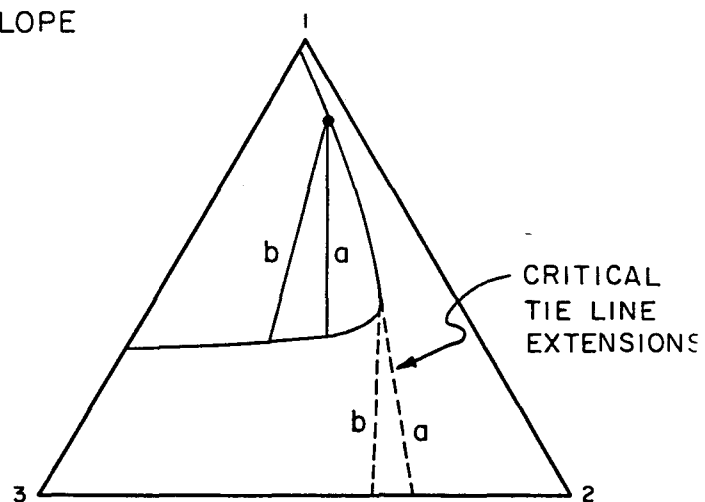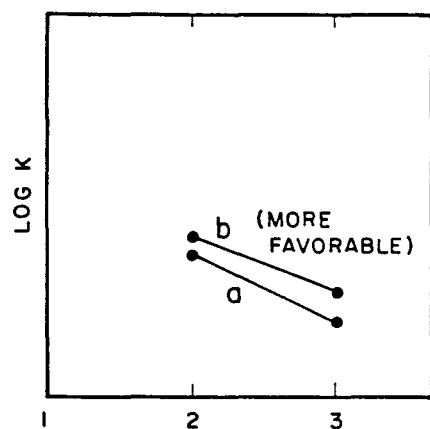
41

a. CASE 1 - CHANGE IN TIE LINE SLOPE

$K_{b1} \gtrsim K_{a1}$

$K_{b2} > K_{a2}$

$K_{b3} < K_{a3}$

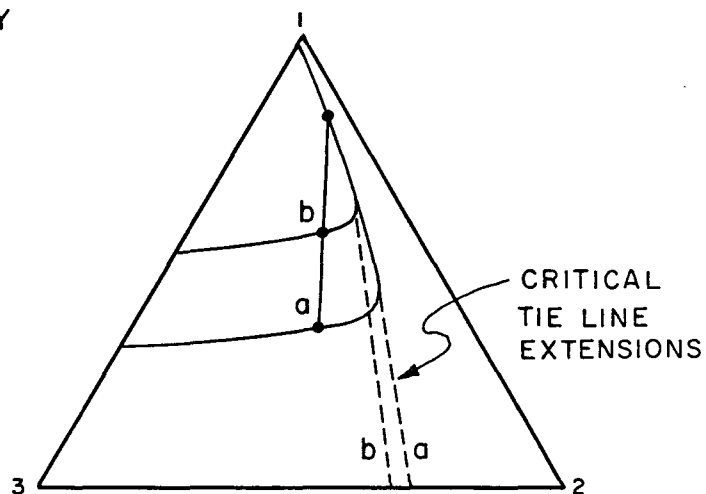## b. CASE 2 - CHANGE IN SOLUBILITY
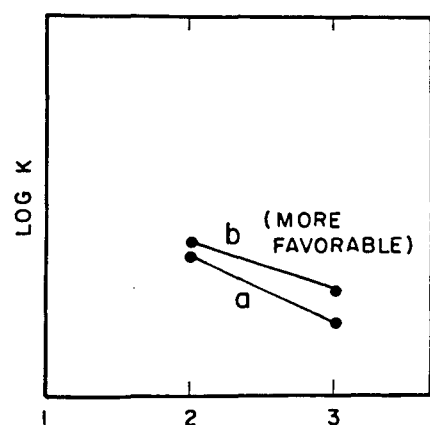

$K_{b1} < K_{a1}$

$K_{b2} > K_{a2}$

$K_{b3} > K_{a3}$

c. CASE 3 - CHANGE IN EXTRACTION

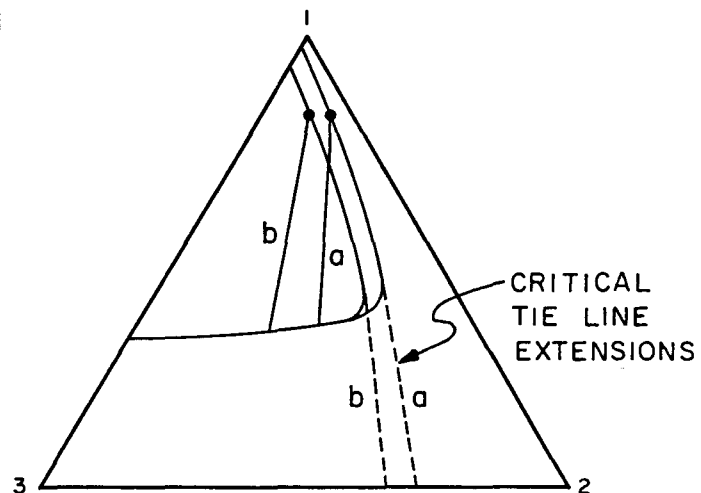$K_{b1} \lesssim K_{a1}$

$K_{b2} > K_{a2}$

$K_{b3} > K_{a3}$

Fig. 2.26   Effects of changes in tie line slope, solubility of component, and extraction of component 3 on partition coefficients.

42

position of the critical tie line. The corresponding equilibrium values indicate that high K-values for the hydrocarbons are more favorable than low ones. Increasing the efficiency of hydrocarbon extraction, as shown in Case 3, also results in behavior more favorable to development of miscibility. Once more the size of the region of tie line extensions decreases as the binodal curve shifts to the left with the increase in hydrocarbon extraction. In this case again, higher hydrocarbon K-values indicate more favorable phase behavior.

This simple analysis of K-value behavior supports the argument based on estimated critical tie lines (Fig. 2.23) that the MMP would be lowest for the branched alkanes, higher for the straight chain alkanes, still higher for the aromatics, and highest for naphthenes. The Maljamar crude oil would have an MMP somewhere between those of normal alkane and naphthenes.

The results presented here do not appear to support an explanation given by Holm and Josendal (1982) for the behavior of slim tube displacements. They compared oil recovery and MMP of a highly paraffinic crude oil with those of the same oil in which intermediate hydrocarbons had been replaced by hydrocarbons from a more aromatic crude oil. They found that "increasing aromaticity correlated with lower miscibility pressure." Based on their observations of slim tube displacement behavior, they argued that "although aromatics and naphthenes are less compatible with CO_2 than paraffin hydrocarbons, aromatics and naphthenes are better solvents for petroleum heavy ends." In the hydrocarbon systems studied here, however, squalane, the heaviest component in each mixture, was extracted less efficiently in the aromatic and naphthenic systems than in the two paraffin systems (Fig. 2.25).

Part of the difference in behavior could be due to the fact that the naphthenic and aromatic hydrocarbons used here are not necessarily equivalent to those found in crude oils. In characterization of crude oils, a compound is referred to as aromatic or naphthenic as long as it contains one ring structure. It may also contain alkyl side chains which could affect how it partitions. For instance, butylbenzene was found to have a higher K-value than benzene (Fig. 2.25). Apparently, the addition of a four carbon side chain improved the solubility of the benzene ring despite the fact that the resulting molecule was larger. In addition, the two intermediate aromatics with their attached alkyl groups partitioned more efficiently into the CO_2-rich phase than their naphthenic counterparts which were composed entirely of polycyclic molecules. It appears, therefore, that higher molecular weight naphthenes with alkyl side chains in place of multiple ring structures might be extracted more effectively. If the aromatic and naphthenic molecules present in a crude oil contain enough relatively small alkyl side chains, then partitioning might be more favorable than was obtained for the systems studied here. According to Hunt (1979), naphthenes account for about 50% of a typical crude oil and tend to be distributed in the heavier fractions. Paraffins are the second most common constituents and generally dominate the gasoline fractions. Aromatics, which rarely make up more than 15% of the oil, also concentrate in the heavier fractions.

Rossini and co-workers (1960) isolated components up to C_{15} of a Ponca City crude oil. The light fraction they investigated accounted for 60% of the

oil and contained 295 compounds. In addition to the normal and branched paraffins the oil contained many different alkyl cyclopentanes, alkyl cyclohexanes, and alkyl benzenes. Molecules composed entirely of cyclic structures were relatively rare compared to the cyclic molecules with alkyl side chains.

Thus, it appears that the hydrocarbon mixtures studied here probably exhibited more sensitivity to molecular type than crude oils would if our speculation that alkyl side chains improve solubility of naphthenes and aromatics in dense CO_2 is correct. Clearly, additional experiments are needed to examine the effects of molecular type in hydrocarbon systems more representative of those found in crude oil.

$CO_2-C_1-C_4-C_{10}$: Measured Phase Compositions and Densities

In the discussion above, the effects of variations in the composition of the oil were considered, but effects of solution gas in the oil were not. It has been observed that addition of solution gas to a crude oil has little effect on the minimum miscibility pressure. For instance, Yellig and Metcalfe's (1980) correlation gives the MMP as a function of temperature only as long as the predicted pressure is above the bubble point pressure of the oil. If not, the bubble point pressure is taken as the MMP. Holm and Josendal (1982) also agreed that the MMP is insensitive to the amount of solution gas present in the oil. It is not obvious why this should be so. While the standard argument is that the light gases move off ahead of the zone where miscibility develops (Holm & Josendal 1982), it is not clear how this fits with standard descriptions of compositional effects in CO_2 floods. Any oil which is at its bubble point pressure has a composition which lies within the region of tie line extensions on a pseudo-ternary diagram of the type used by Hutchinson and Braun (1961) in their description of multiple contact miscibility, since the oil composition lies on the binodal curve. Thus, according to the simple theory of the generation of miscibility, such an oil would not be multiple contact miscible with CO_2.

To investigate a model system containing solution gas, CMC experiments were performed for several systems containing CO_2, methane (C_1), butane (C_4) and decane (C_{10}). Phase composition and density data are reported here for four ternary systems and one quaternary system, all at 160°F and 1250 psia:

$$(1) \quad CO_2-C_4-C_{10}$$

$$(2) \quad C_1-C_4-C_{10}$$

$$(3) \quad CO_2-C_1-C_{10}$$

$$(4) \quad CO_2-C_1-C_4$$

$$(5) \quad CO_2-C_1-C_4-C_{10}$$

Additional experimental details are reported elsewhere (Silva et al 1983). Data for the $CO_2-C_4-C_{10}$ system were reported by Metcalfe and Yarborough (1979)

and by Orr and Silva (1983). The C_1-C_4-C_{10} system was studied by Reamer, Fiskin and Sage (1951). The results reported here for the CO_2-C_1-C_{10}, CO_2-C_1-C_4 and CO_2-C_1-C_4-C_{10} systems are new. Data for the CO_2-C_4, C_1-C_{10} and C_1-C_4 systems are given by Sage and Lacey (1955) and for the CO_2-C_{10} system by Reamer and Sage (1963).

Tables 2.10-2.13 summarize all of the phase composition and density data available for the four ternary systems. Figs. 2.27-2.30 give the same data on ternary phase diagrams. Agreement between the values obtained with the continuous multiple contact experiments and those obtained by static equilibrium measurements is good. Table 2.14 reports compositions and densities for phases generated with four components present. Figs. 2.31a and b show the data plotted on a pair of quaternary diagrams. The two figures are stereo pairs. When viewed with a stereoscope, they produce a three-dimensional image which shows clearly the locations of tie lines in the interior of the tetrahedron.

The phase composition and density data reported form the basis for an examination of the effects of methane on displacement performance, to be attempted in subsequent work. The data also provide additional confirmation that the CMC experiment can generate phase composition measurements of reasonable accuracy. The fact that density data were also obtained may prove useful for the development and testing of some equations of state (Kuan et al 1983).

CO_2-C_1-C_4-C_{10}: Calculated Phase Compositions and Densities

While the CMC technique allows relatively rapid collection of equilibrium phase composition and fluid property data, experimental investigations of the sort described above still require substantial investment of time, equipment and effort. Thus, the range of temperature, pressures and compositions which can be investigated is necessarily limited. If sufficiently accurate, an equation of state can be used to interpolate existing data and to examine a wider range of temperatures, pressures and compositions. In this section, we compare phase compositions and densities calculated with the Peng-Robinson equation of state (PREOS, 1976) for the CO_2-C_1-C_4-C_{10} system. The program used for the calculations was obtained from the Gas Processors Association. It was modified to install a Newton-Raphson iteration along the lines described by Fussell and Yanosik (1978), in addition to the successive substitution used in the original version. For most of the computations described below, the Newton-Raphson iteration converged much more rapidly than successive substitutions, although it required a more accurate initial guess for convergence than did successive substitutions. In all but a few cases, a sufficiently accurate initial guess could be generated by performing a small number of successive substitution iterations and then switching to Newton-Raphson iteration. In some cases, particularly those involving liquid-liquid (L_1-L_2) or liquid-liquid-vapor (L_1-L_2-V) phase behavior, either iterative technique may converge to more than one solution to the equations, depending on the initial guess. In those calculations, the correct solution was identified by selecting the one with the lowest Gibbs free energy as described by Baker, Pierce and Luks (1982).

Table 2.10   Measured Compositions and Densities for the
$CO_2-C_4-C_{10}$ System at 160°F and 1250 psia

	Lower Phase				Upper Phase		
CO_2	C_4	C_{10}	ρ (g/cm³)	CO_2	C_4	C_{10}	ρ (g/cm³)
From CMC							
0.644	0.285	0.071	0.5150	0.811	0.178	0.012	0.2568
0.644	0.281	0.075	0.5157	0.874	0.123	0.004	0.2600
0.640	0.281	0.079	0.5210	0.880	0.118	0.002	0.2600
0.639	0.278	0.083	0.5206	0.887	0.112	0.002	0.2572
0.637	0.273	0.090	0.5259	0.892	0.106	0.002	0.2537
0.642	0.266	0.092	0.5227	0.892	0.105	0.003	0.2533
0.654	0.254	0.091	0.5248	0.890	0.108	0.003	0.2449
0.640	0.249	0.111	0.5283	0.896	0.103	0.001	0.2392
0.638	0.242	0.120	0.5248	0.905	0.094	0.001	0.2354
0.628	0.181	0.190	–	0.931	0.067	0.003	–
0.633	0.176	0.191	–	0.937	0.062	0.001	–
0.620	0.167	0.213	–	0.939	0.060	0.001	–
From Metcalfe & Yarborough							
0.6090	0.0927	0.2983	–	0.9679	0.0291	0.0030	–
				0.9702	0.0269	0.0028	–
0.6023	0.1593	0.2384	–	0.9434	0.0528	0.0038	–
0.6231	0.2191	0.1578	–	0.9169	0.0795	0.0036	–
				0.9146	0.0816	0.0038	–
0.6520	0.2745	0.0735	–	0.8759	0.1195	0.0046	–
				0.8735	0.1221	0.0044	–
0.6727	0.2943	0.0330	–	0.8469	0.1497	0.0034	–

Table 2.11 Measured Compositions and Densities for the CO_2-C_1-C_{10} System at 160°F and 1250 psia

Lower Phase				Upper Phase			
CO_2	C_1	C_{10}	ρ (g/cm³)	CO_2	C_1	C_{10}	ρ (g/cm³)
Samples Generated During CO_2 Injection							
0.017	0.340	0.643	0.6509	0.049	0.951	–*	0.0519
0.129	0.250	0.621	0.6654	0.279	0.719	0.002	0.0825
0.219	0.206	0.575	0.6733	0.400	0.600	–	0.0971
0.299	0.165	0.536	0.6824	0.515	0.485	–	0.1139
0.346	0.128	0.525	0.6889	0.620	0.380	–	0.1246
0.390	0.097	0.512	0.6961	0.694	0.306	–	0.1372
0.451	0.079	0.470	0.7012	0.742	0.258	–	0.1461
0.450	0.063	0.488	0.7041	0.777	0.223	–	0.1526
0.478	0.055	0.467	0.7070	0.811	0.189	–	0.1594
0.507	0.044	0.449	0.7099	0.846	0.154	–	0.1648
0.511	0.036	0.453	0.7103	0.890	0.110	–	0.1698
0.570	0.032	0.399	0.7136	0.904	0.096	–	0.1781
Samples Generated During Methane Injection							
0.312	0.143	0.545	0.686	0.520	0.477	0.003	0.1089
0.243	0.165	0.592	0.681	0.423	0.572	0.005	0.0968
0.204	0.195	0.601	0.677	0.352	0.645	0.003	0.0820

*dash indicates that the amount of decane in the upper phase was not measured

Table 2.12   Measured Compositions and Densities for the
              CO_2-C_1-C_4 System at 160°F and 1250 psia

	Lower Phase				Upper Phase		
CO_2	C_1	C_4	ρ (g/cm³)	CO_2	C_1	C_4	ρ (g/cm³)
0.011	0.348	0.641	0.4176	0.047	0.715	0.238	0.1243
0.064	0.320	0.616	0.4224	0.095	0.669	0.236	0.1317
0.123	0.290	0.587	0.4277	0.183	0.579	0.238	0.1454
0.178	0.256	0.566	0.4327	0.265	0.504	0.231	0.1587
0.231	0.227	0.542	0.4390	0.337	0.455	0.208	0.1727
0.280	0.200	0.520	0.4468	*	*	*	*
0.325	0.178	0.497	0.4511	*	*	*	*
0.374	0.171	0.455	0.4521	0.473	0.296	0.231	0.2119

*Temporary loss of temperature control downstream of cell
resulted in loss of compositional measurements

Table 2.13   Measured Compositions and Densities for the
              C_1-C_4-C_{10} System at 160°F and 1250 psia

	Lower Phase				Upper Phase		
C_1	C_4	C_{10}	ρ (g/cm³)	C_1	C_4	C_{10}	ρ (g/cm³)
From Sage & Lacey							
0.298	0.000	0.702	–	0.998	0.000	0.0023	–
0.292	0.142	0.566	–	0.964	0.033	0.0024	–
0.291	0.283	0.425	–	0.927	0.070	0.0025	–
0.296	0.423	0.282	–	0.886	0.111	0.0026	–
0.308	0.553	0.138	–	0.834	0.164	0.0021	–
0.348	0.652	0.000	–	0.759	0.241	0.0000	–
From CMC							
0.303	0.452	0.245	0.558	0.832	0.141	0.0049	0.0867
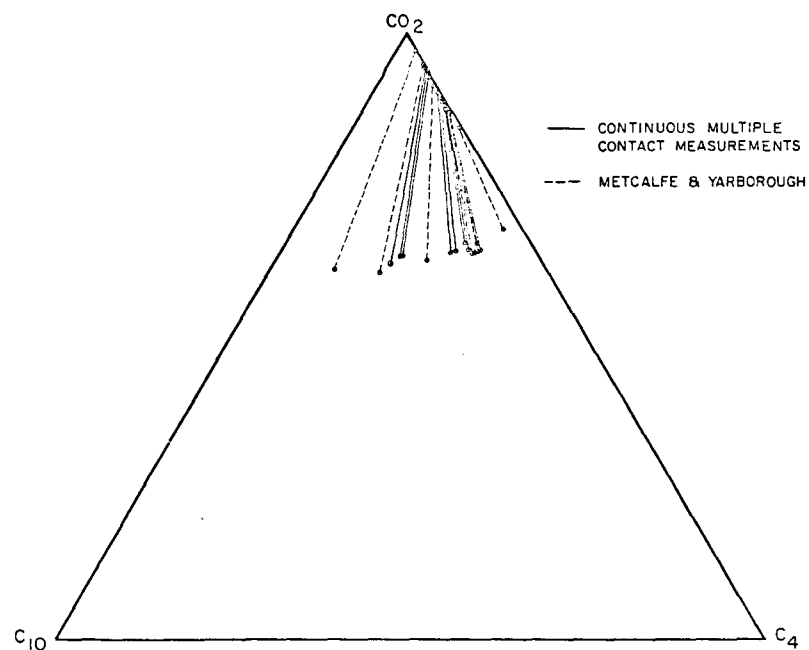
Fig. 2.27 Measured phase compositions for CO_2-C_4-C_{10} mixtures at 160°F and 1250 psia.
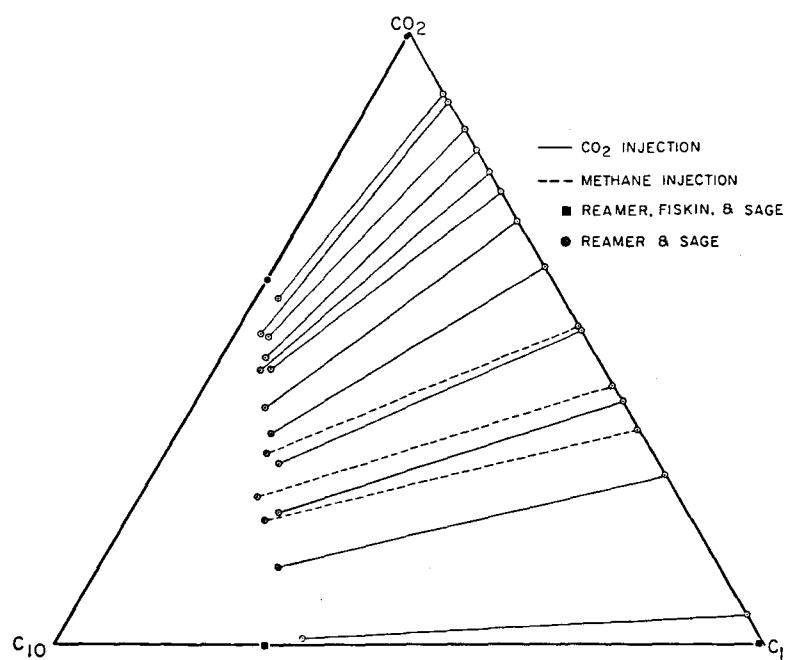
Fig. 2.28 Measured phase compositions for CO_2-C_1-C_{10} mixtures at 160°F and 1250 psia.
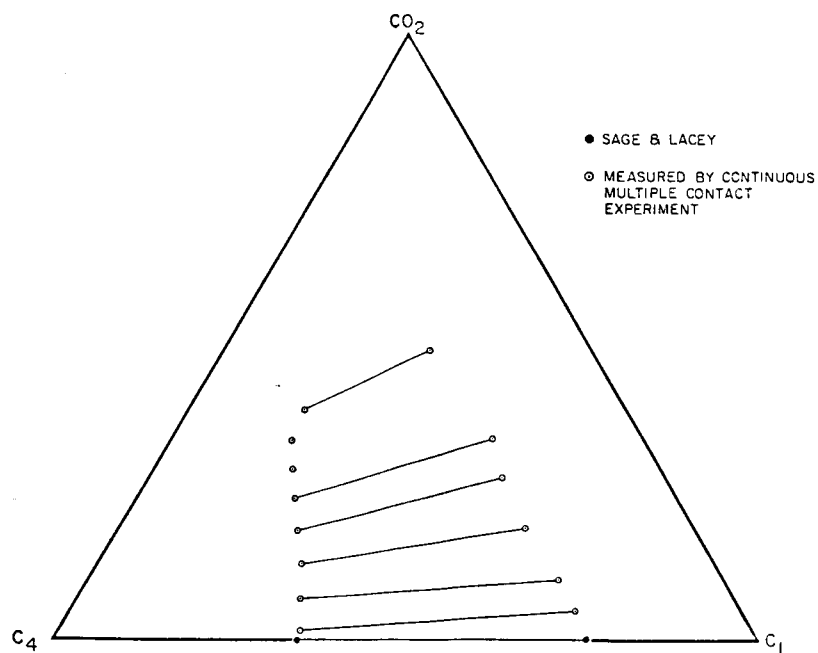
Fig. 2.29   Measured phase compositions for CO_2-C_1-C_4 mixtures at 160°F and 1250 psia.
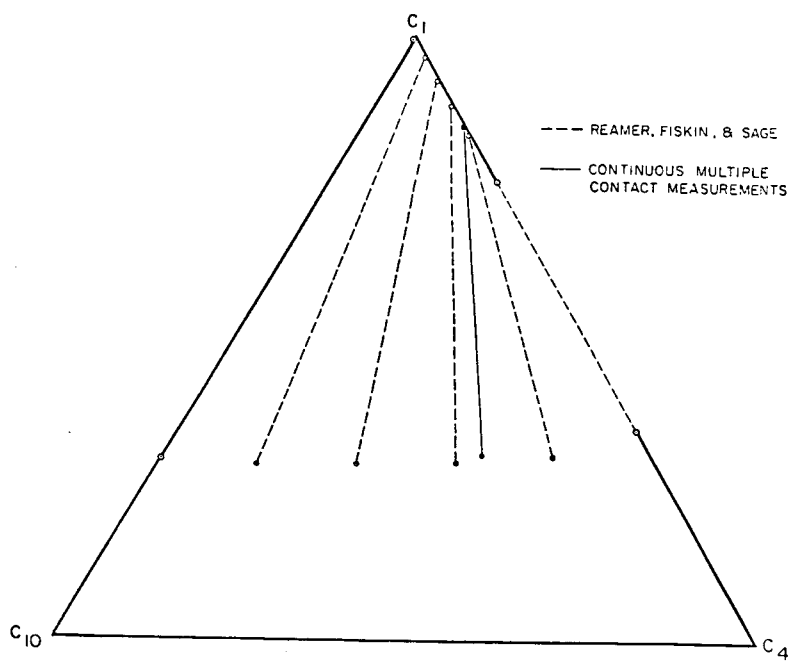
Fig. 2.30   Measured phase compositions for C_1-C_4-C_{10} mixtures at 160°F and 1250 psia.

Table 2.14   Measured Compositions and Densities for the
CO_2-C_1-C_4-C_{10} System at 160°F and 1250 psia

		Lower Phase					Upper Phase		
CO_2	C_1	C_4	C_{10}	ρ (g/cm^3)	CO_2	C_1	C_4	C_{10}	ρ (g/cm^3)
0.000	0.303	0.452	0.245	0.5586	0.000	0.851	0.144	0.005	0.0867
0.045	0.268	0.405	0.282	0.5743	0.174	0.686	0.134	0.005	0.1135
0.159	0.196	0.351	0.294	0.5912	0.340	0.528	0.128	0.004	0.1375
0.259	0.162	0.349	0.230	0.6074	0.471	0.402	0.121	0.006	0.1544
0.329	0.119	0.320	0.232	0.6232	0.576	0.306	0.113	0.005	0.1705
0.398	0.094	0.271	0.237	0.6387	0.664	0.228	0.103	0.005	0.1803

Table 2.15   Binary Interaction Parameters
Used in the Peng-Robinson EOS

	CO_2	C_1	n-C_4
n-C_{10}	0.110	0.000	0.000
n-C_4	0.130	0.000	
C_1	0.100		
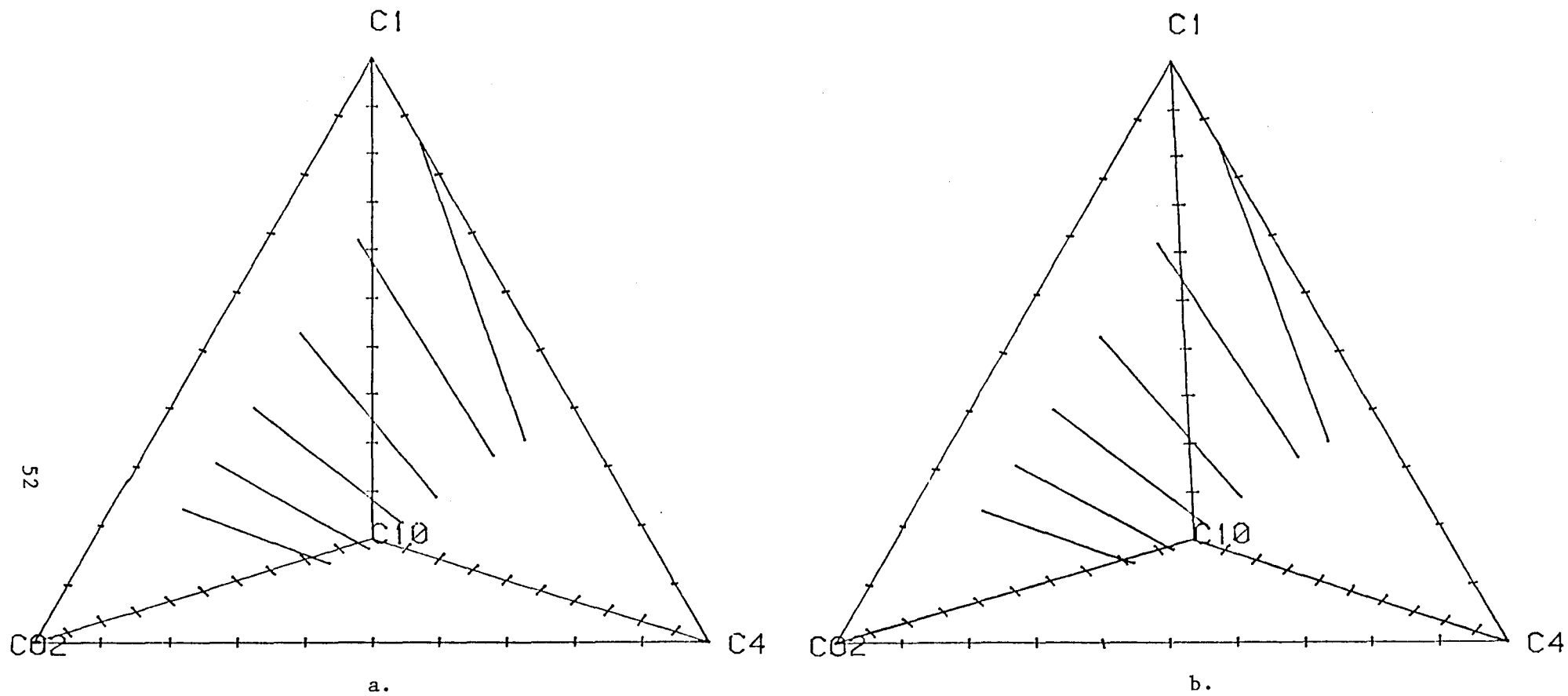
Fig. 2.31   Measured phase compositions for CO_2-C_1-C_4-C_{10} mixtures at 160°F and 1250 psia.

Results of the calculations are compared with measured phase compositions for each of the binary pairs in Figs. 2.32-2.35. Binary interaction parameters used in the calculations are given in Table 2.15. While there are some regions of pressure and composition, for instance the critical region for the CO_2-C_{10} pair (Fig. 2.32) in which the agreement between calculation and experiment could be improved, the overall agreement is good. Calculated phase compositions also agreed well for the four ternary systems, as is shown in Figs. 2.36-2.39. The calculated two-phase region was slightly larger than the measured version for the CO_2-C_4-C_{10} system (Fig. 2.36) and slightly smaller for the C_1-C_4-C_{10} (Fig. 2.37) and CO_2-C_1-C_4 (Fig. 2.39) systems. Calculated and measured densities are compared for the three ternary systems for which density measurements were made in the CMC experiment in Figs. 2.40-2.42. Vapor densities agreed very well for all the systems. Calculated liquid densities were 10-18% high for the CO_2-C_4-C_{10} system (Fig. 2.40), about 7% low for CO_2-C_1-C_4 mixtures (Fig. 2.41), and 4-7% low for the CO_2-C_1-C_{10} system (Fig. 2.42).

Figs. 2.43a and b compare calculated and measured compositions for the quaternary system. Again, agreement is good. In fact, the agreement for all of the binary, ternary and quaternary systems is good enough to suggest that the PREOS can be used to interpolate the existing data and to examine the evolution of the phase diagrams with changes in temperature or pressure. As with any extrapolation, of course, there is no guarantee that phase compositions calculated for conditions substantially different from those at which experimental confirmation was obtained will be as accurate. Nevertheless, the agreement observed for the binary systems over a wide range of pressures suggests that reasonable qualitative and quantitative agreement is likely.

The evolution of phase diagrams for the quaternary system with increasing pressure at 160°F is shown in Figs. 2.44-2.46. In these diagrams, only the ternary faces of the quaternary diagram are shown, unfolded so that they can be seen clearly. At 1000 psia (Fig. 2.44), the two-phase region is a continuous band across the diagram. There are no critical points because the pressure is low enough that all of the binary pairs are immiscible (Figs. 2.32-2.35). At 1500 psia (Fig. 2.45), CO_2 and C_4 are miscible, and a locus of critical compositions connects the plait points on the CO_2-C_1-C_4 and CO_2-C_4-C_{10} faces through the interior of the tetrahedron. At 2000 psia (Fig. 2.46), C_1 is miscible with C_4 and the CO_2-C_{10} binary pair is very close to its calculated critical pressure. Thus, the critical locus connects the critical point on the CO_2-C_{10} edge of the tetrahedron to a plait point just inside the C_1-C_4-C_{10} ternary face. The approximate location of that critical locus and the behavior of tie lines in the interior of the diagram can be seen in the stereo pair shown in Figs. 2.47a and b. With additional increases in pressure, the two-phase region continues to shrink, disappearing finally at the critical pressure of the C_1-C_{10} pair.

Calculated Phase Behavior: L_1-L_2 and L_1-L_2-V Systems

Scott and van Konynenburg (1970) showed that the qualitative features of complex liquid-liquid (L_1-L_2) and liquid-liquid-vapor (L_1-L_2-V) phase behavior

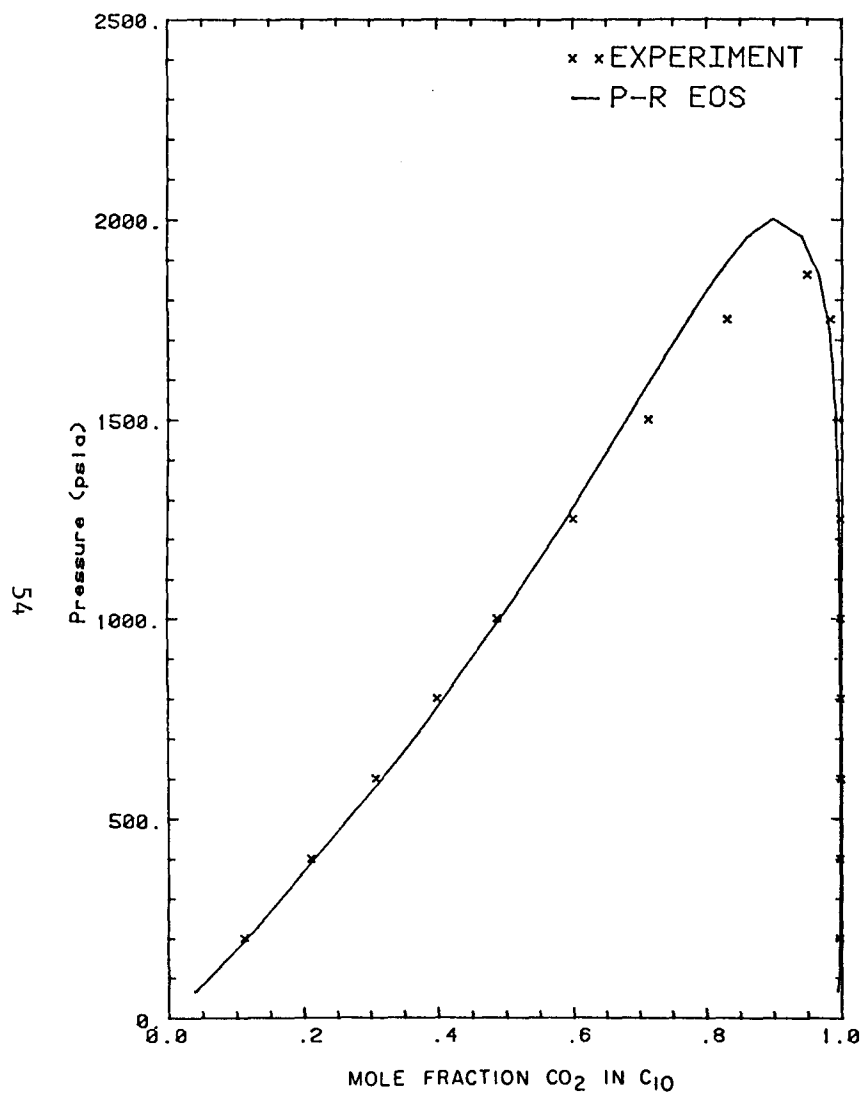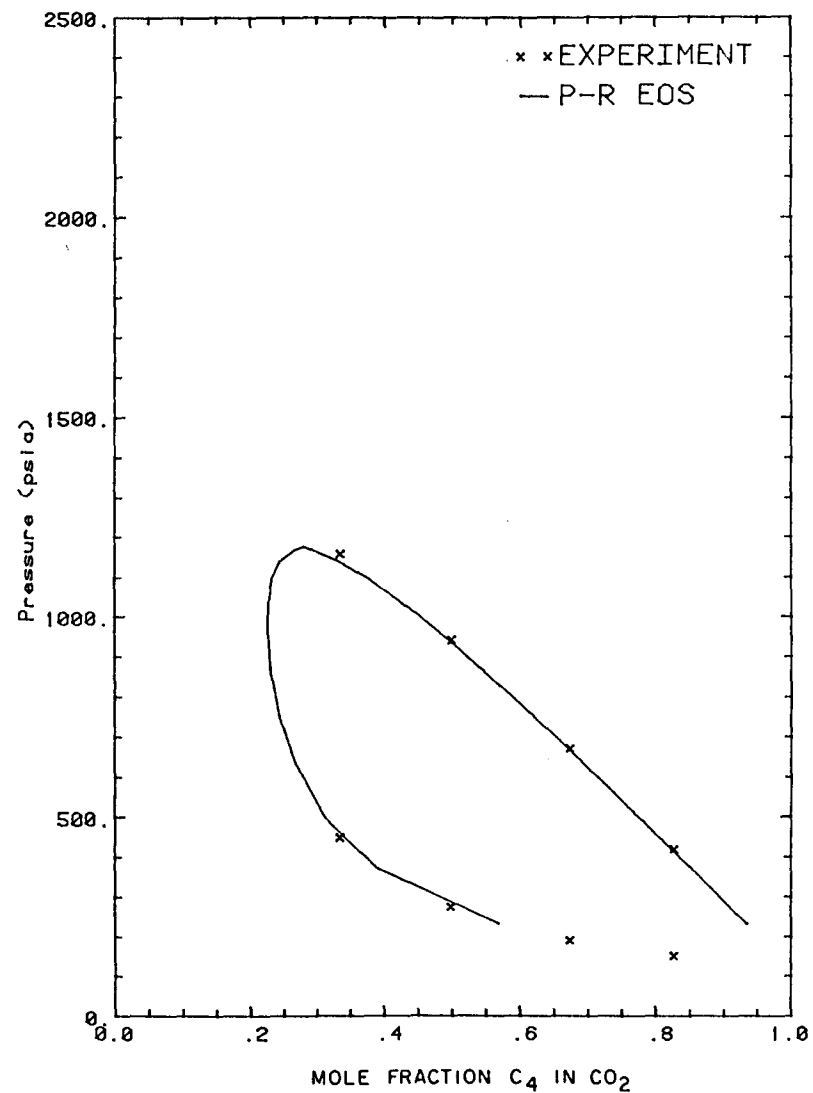Fig. 2.32   Phase compositions for CO_2-C_{10} mixtures at 160°F.

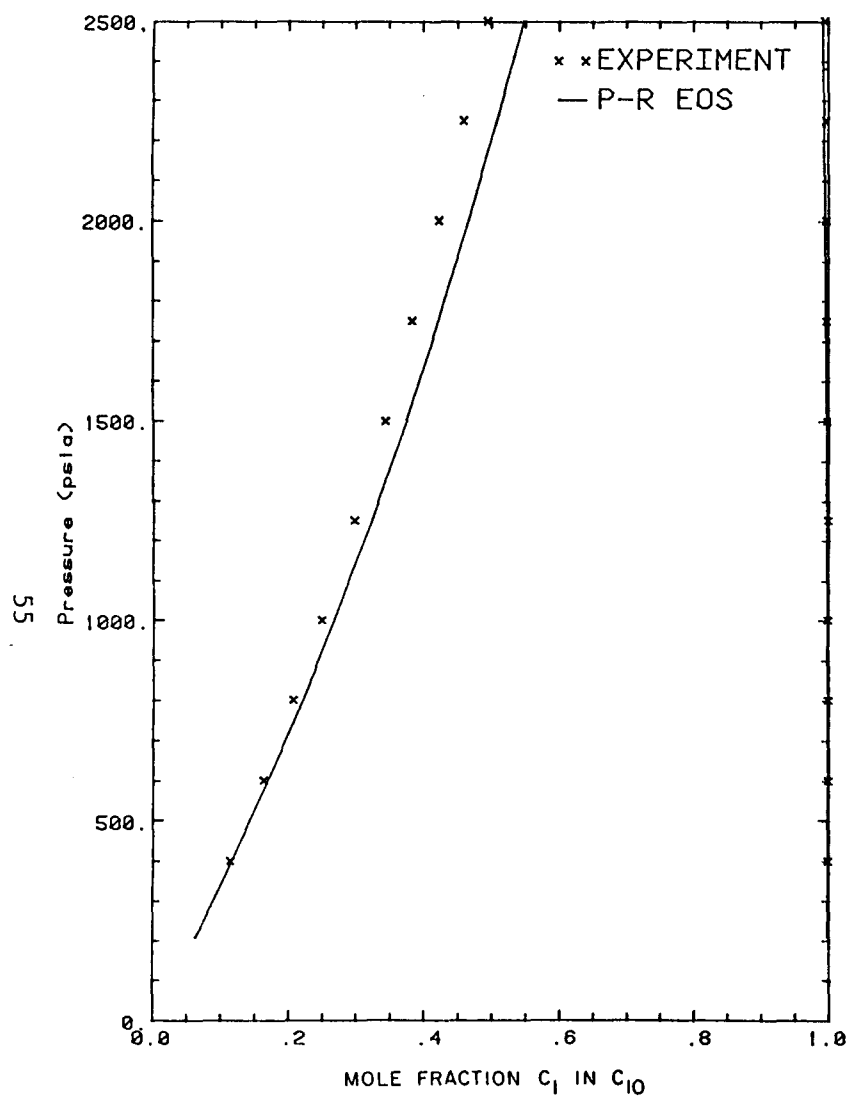Fig. 2.33   Phase compositions for CO_2-C_4 mixtures at 160°F.

54

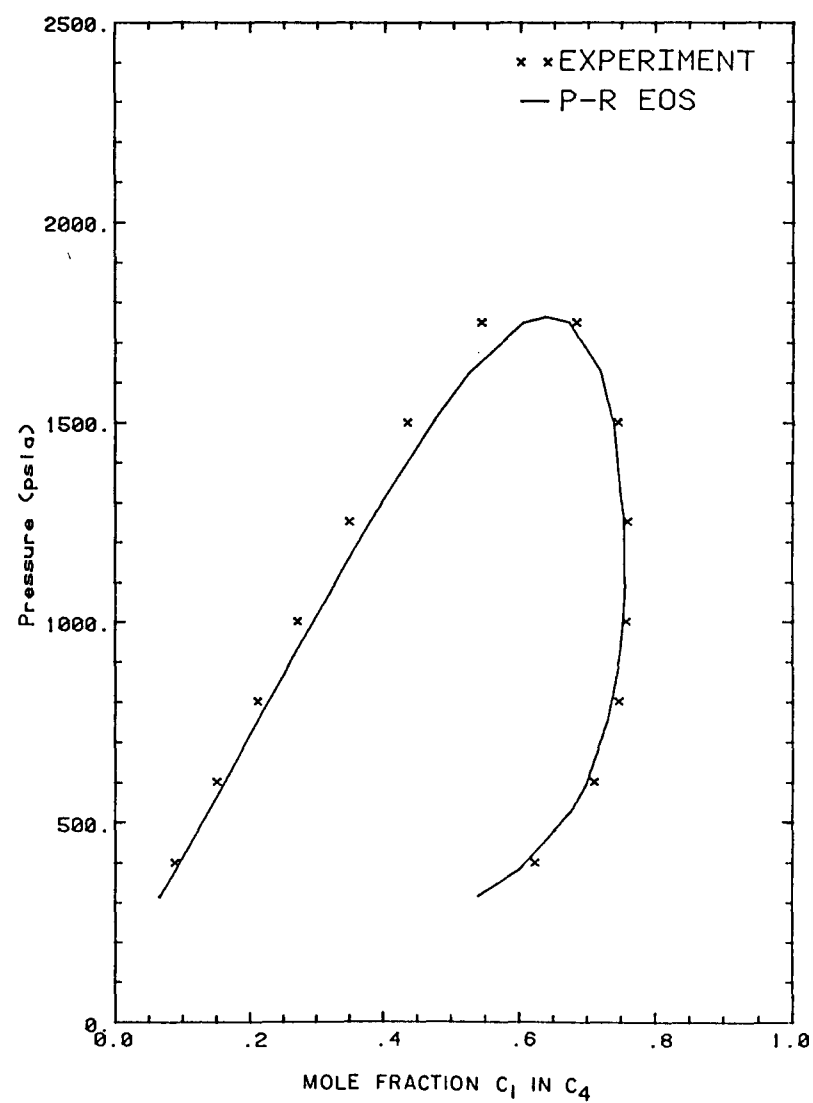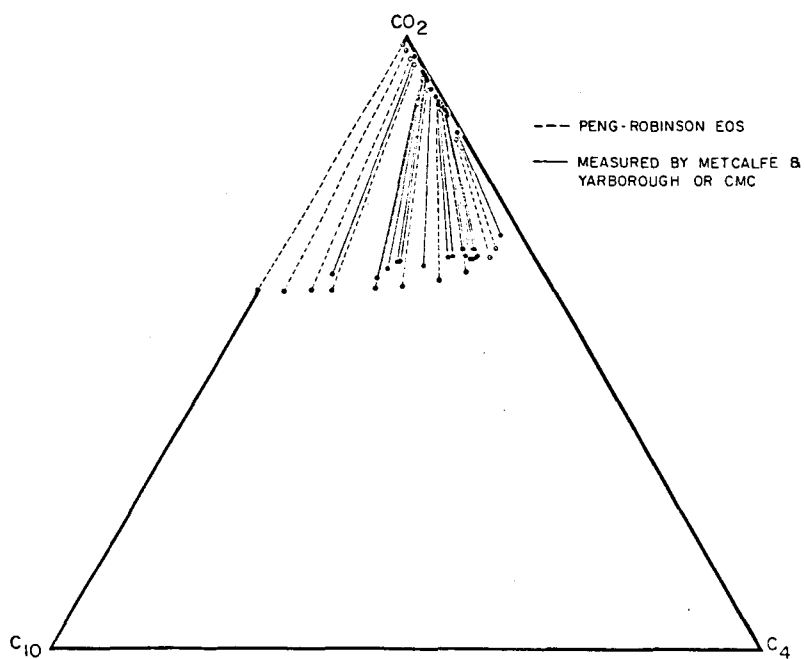Fig. 2.34 Phase compositions for C_1-C_{10}
mixtures at 160°F.

Fig. 2.35 Phase compositions for C_1-C_4
mixtures at 160°F.

55

Fig. 2.36   Comparison of calculated and measured phase compositions
for CO_2-C_4-C_{10} mixtures at 160°F and 1250 psia.
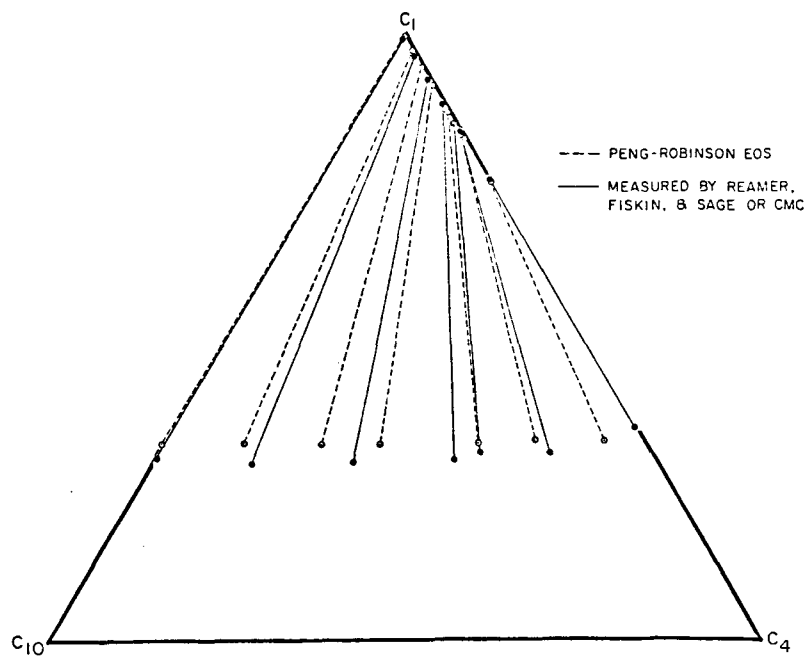
Fig. 2.37   Comparison of calculated and measured phase compositions
for C_1-C_4-C_{10} mixtures at 160°F and 1250 psia.
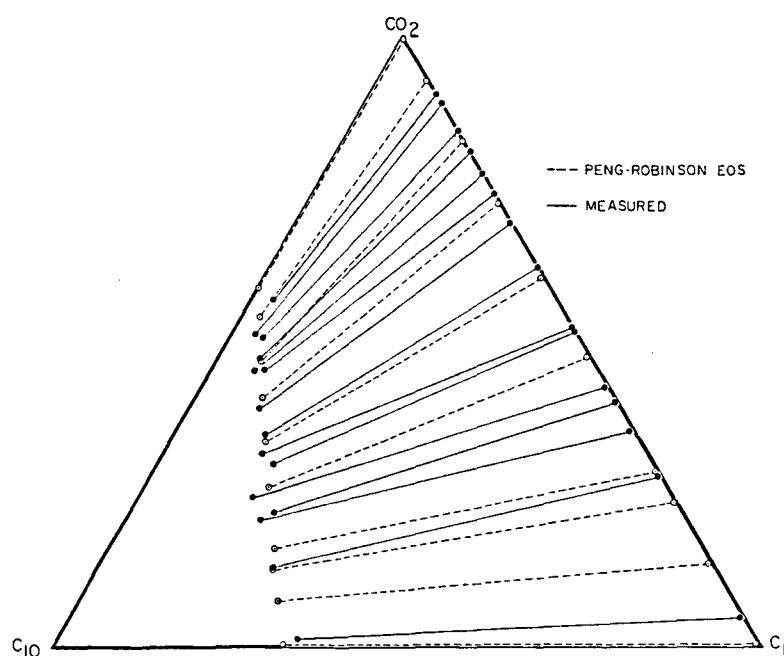
Fig. 2.38   Comparison of calculated and measured phase compositions for CO_2-C_1-C_{10} mixtures at 160°F and 1250 psia.
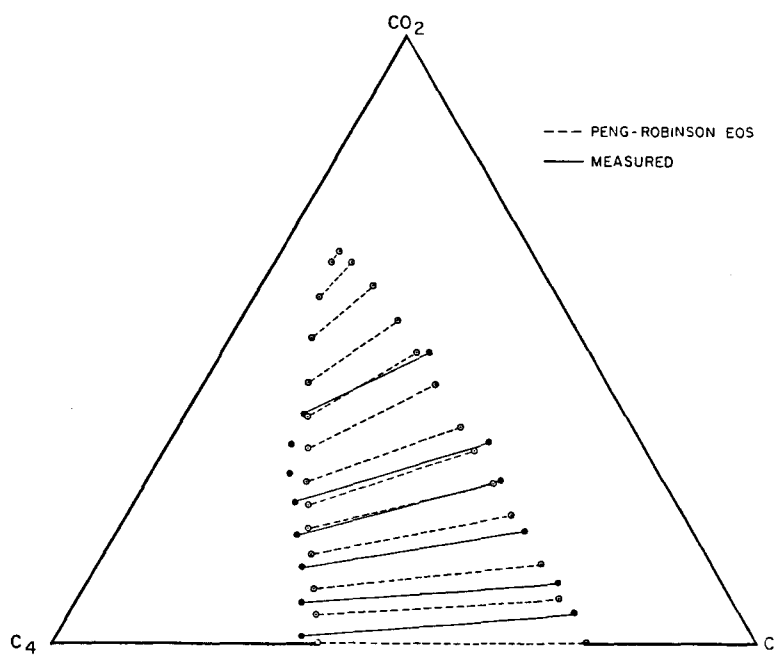
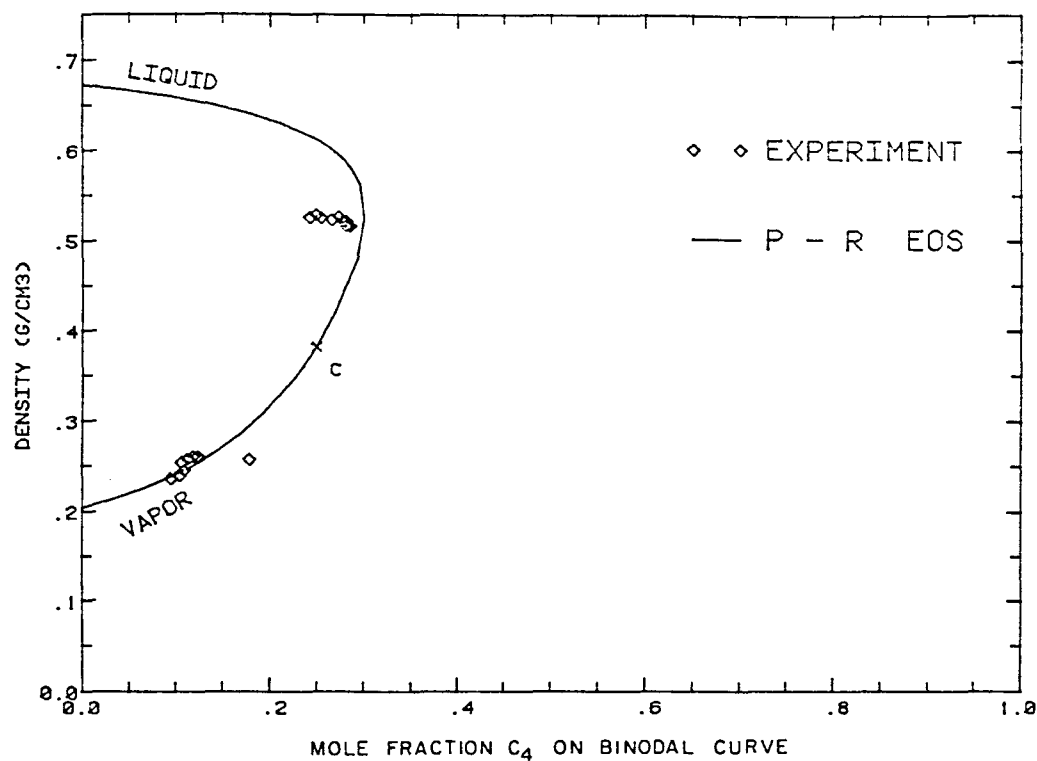Fig. 2.39   Comparison of calculated and measured phase compositions for CO_2-C_1-C_4 mixtures at 160°F and 1250 psia.

Fig. 2.40   Comparison of calculated and measured densities for CO_2-C_4-C_{10} mixtures at 160°F and 1250 psia.

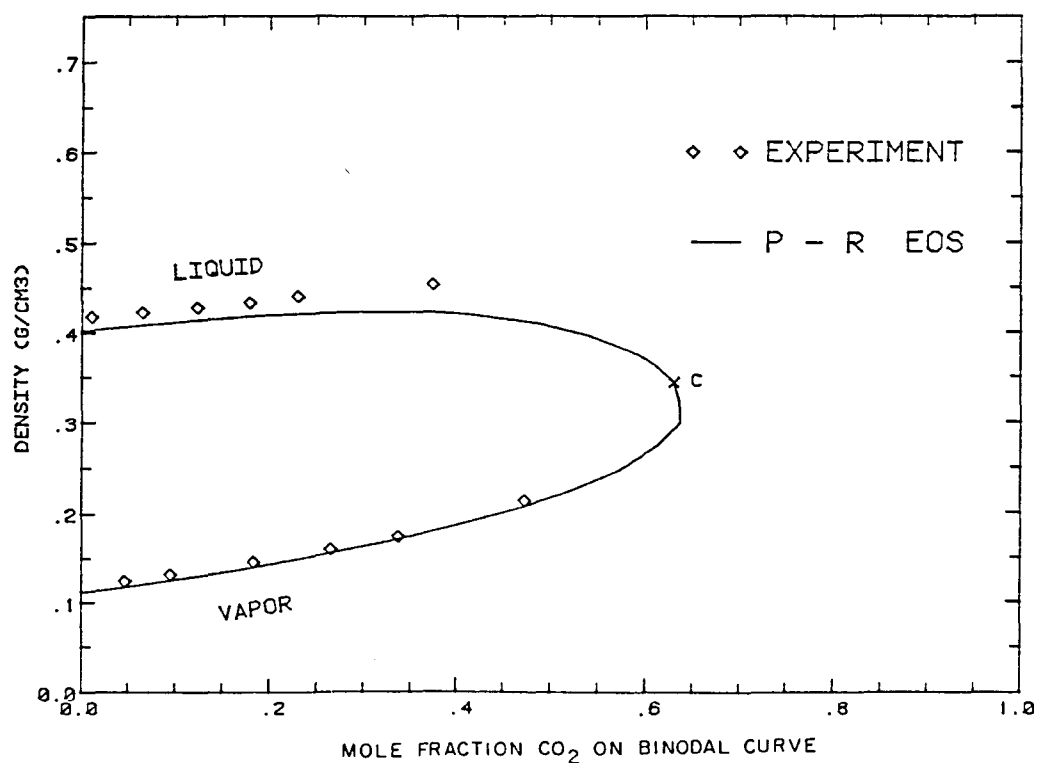
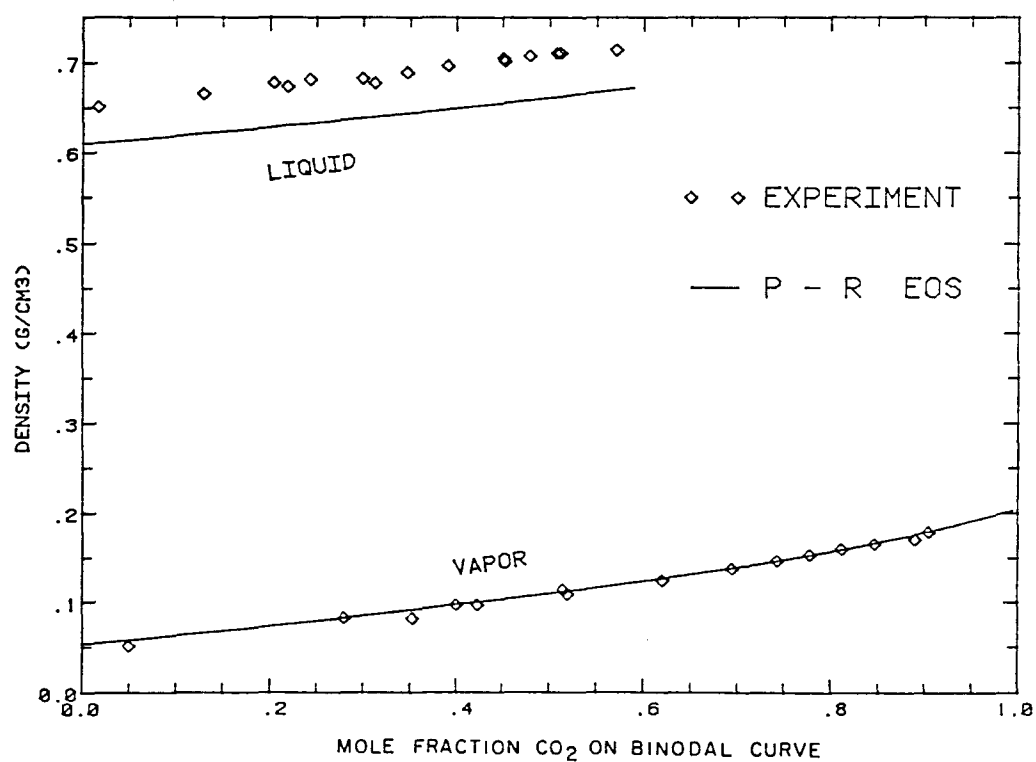Fig. 2.41   Comparison of calculated and measured densities for CO_2-C_1-C_4 mixtures at 160°F and 1250 psia.

Fig. 2.42 Comparison of calculated and measured densities for CO_2-C_1-C_{10} mixtures at 160°F and 1250 psia.

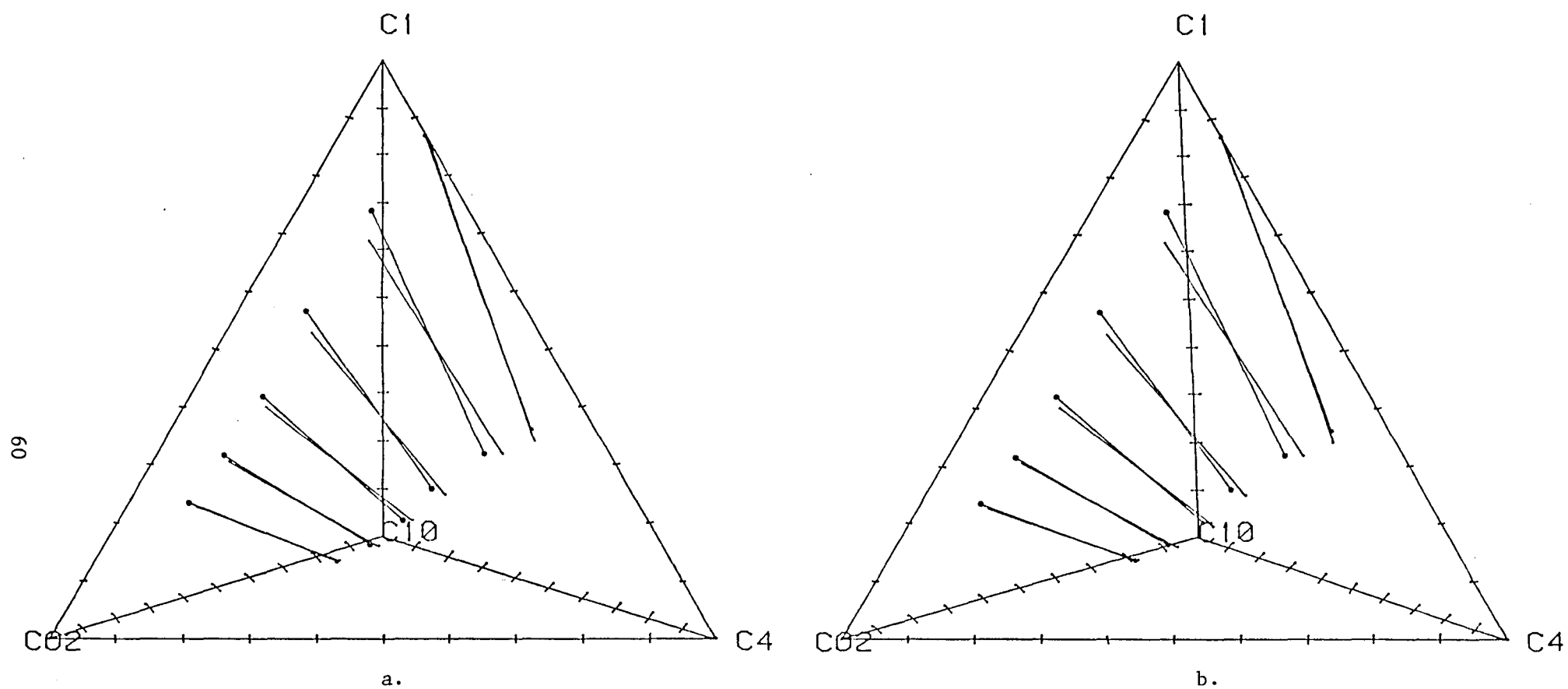Fig. 2.43   Comparison of calculated and measured phase compositions for CO_2-C_1-C_4-C_{10} mixtures at 160°F and 1250 psia.
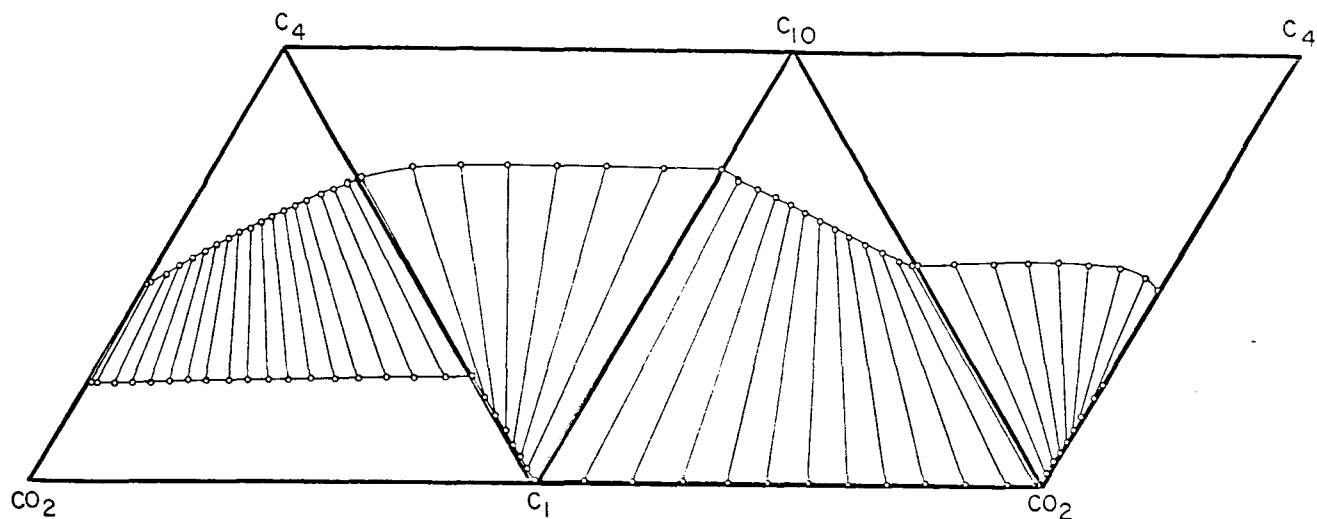
Fig. 2.44   Calculated phase compositions for CO_2-C_1-C_4-C_{10} mixtures at 160°F and 1000 psia.
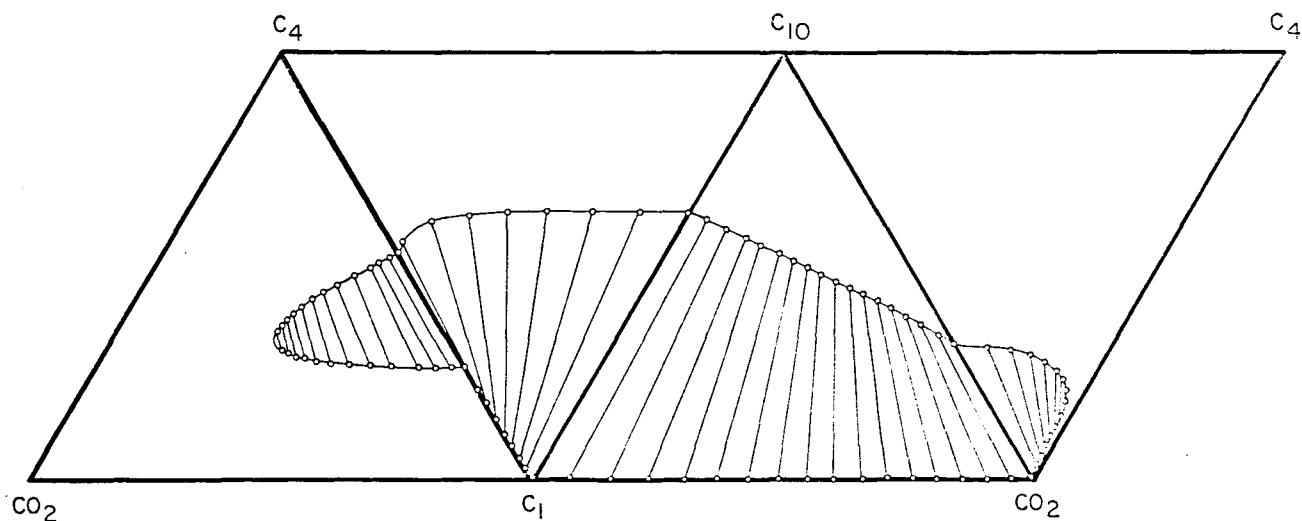
Fig. 2.45   Calculated phase compositions for CO_2-C_1-C_4-C_{10} mixtures at 160°F and 1500 psia.

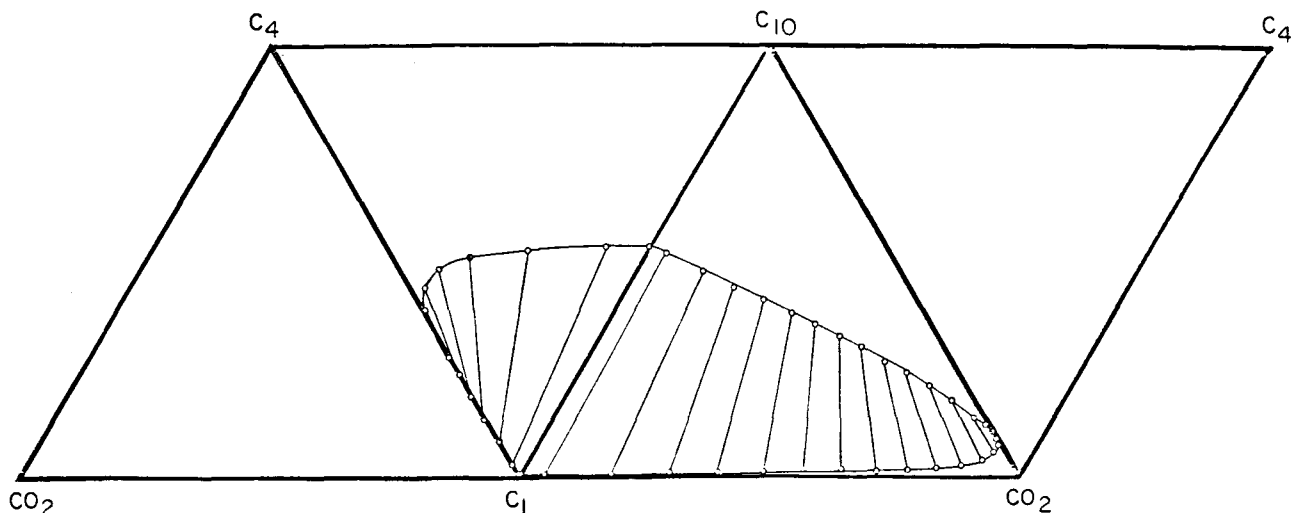

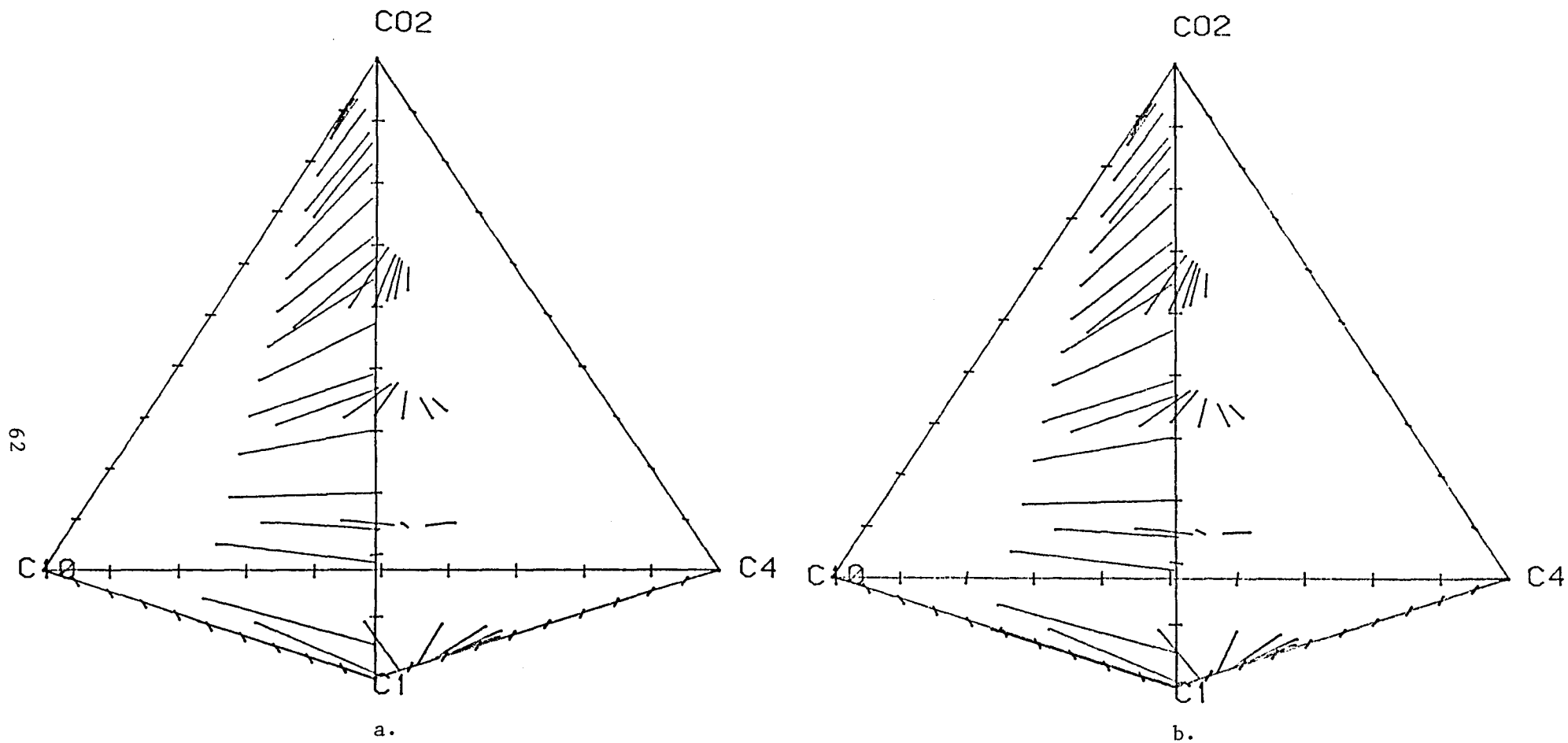Fig. 2.46   Calculated phase compositions for CO_2-C_1-C_4-C_{10} mixtures at 160°F and 2000 psia.

Fig. 2.47   Calculated phase compositions for CO_2-C_1-C_4-C_{10} mixtures at 160°F and 1250 psia.

are predicted by van der Waals equation, the simplest of the cubic equations of state. Fussell (1979) obtained reasonable predictions of phase volumes with a modified Redlich-Kwong EOS for a CO_2-crude oil system which formed L-V, L_1-L_2-V and L_1-L_2 mixtures as the pressure was increased (see §2.1). Mehra, Heidemann and Aziz (1982) showed that the PREOS predicted a three-phase region for the CO_2-C_3-C_{16} ternary system studied by Meldrum and Nielsen (1955), though there were some differences between calculated and measured phase compositions. In this section, we examine the performance of the PREOS for two additional systems which show L_1-V, L_1-L_2-V, L_1-L_2 and liquid-dense phase equilibria: CO_2-normal hexadecane (C_{16}) and CO_2-C_1-C_{16}. Data for the CO_2-C_{16} system were reported by Stewart and Nielsen (1954) and for the CO_2-C_1-C_{16} system by Orr, Lien and Pelletier (1981).

Figs. 2.48 and 2.49 compare calculated and measured phase compositions for CO_2-C_{16} mixtures at 70 and 90°F. For a review of the qualitative features of such phase diagrams see Orr and Jensen (1984). In both cases, the solubility of CO_2 in C_{16} was predicted with reasonable accuracy. The calculated pressures at which three phases coexisted were nearly identical with the observed values, and the compositions of the three coexisting phases also matched closely the observed values. Though details of the small L_2-V regions at very high CO_2 concentrations and pressures just above the three-phase pressure cannot be seen on the scale of Figs. 2.48 and 2.49, the EOS did predict the existence of those regions. The small L_2-V region disappears, with increasing temperature, at an upper critical end point (UCEP), where the L_2 and V phases are identical (Schneider et al 1967; Schneider 1968; Orr, Yu & Lien 1981; Orr & Jensen 1984). While the exact temperature and pressure of the UCEP was not calculated (nor has it been measured), the PREOS does produce the right qualitative behavior. Fig. 2.50 shows a calculated CO_2-C_{16} phase diagram at 110°F. At the higher temperature, no three-phase pressure was found. Instead, mixtures at high concentrations formed a liquid in equilibrium with a low density fluid (vapor) at low pressures and a liquid in equilibrium with a dense fluid (L-F) at high pressures. Similar behavior is observed in CO_2-crude oil systems (Orr, Yu & Lien 1981; Orr & Jensen 1984).

Results of computations performed for CO_2-C_1-C_{16} mixtures at 90°F are shown in Figs. 2.51-2.56. At 1000 psia (Fig. 2.51), no three-phase region was found. The three-phase region first appears, with increasing pressure, at the CO_2-C_{16} side of the diagram at the three-phase pressure for the CO_2-C_{16} pair (about 1090 psia; Stewart & Nielsen 1954; Orr, Lien & Pelletier 1981; Orr & Jensen 1984). With additional pressure increases, the three-phase region moves into the interior of the ternary diagram as more C_1 is compressed into the liquid phases, as is shown in Fig. 2.52. Measured (Orr, Lien & Pelletier 1981) and calculated compositions for the three-phase region are compared in Fig. 2.52, and a closer view of the small L_2-V region and the measured and calculated compositions of the L_2 and V phases in the three-phase region is given in Fig. 2.53. The L_1 composition reported by Orr, Lien and Pelletier (1981) is not consistent with the L_1 composition reported by Stewart and Nielsen (1954) or with the calculated value and hence appears to be in error.

The three-phase region disappears at a critical tie line (Orr, Lien & Pelletier 1981; Orr & Jensen 1984), at which the L_2 and V phases become
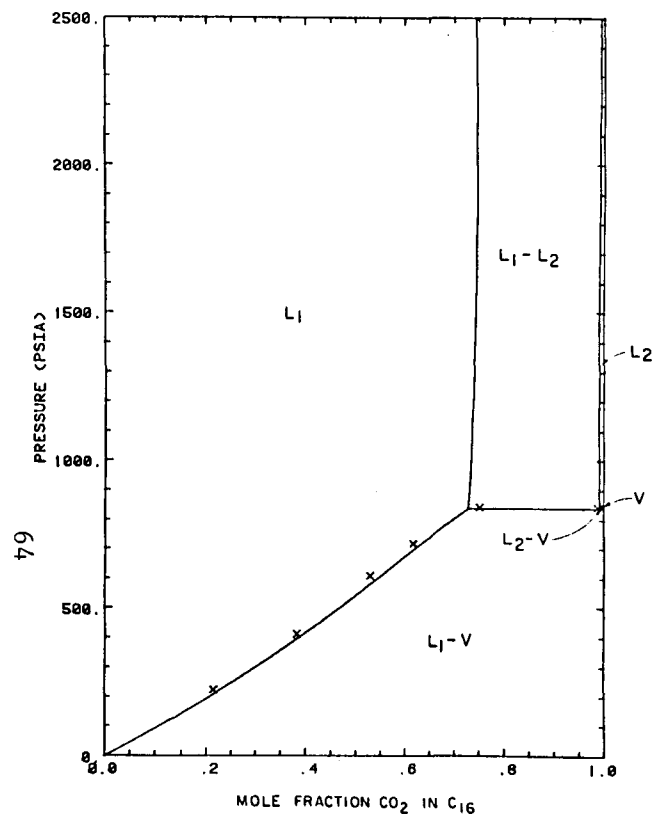
Fig. 2.48 Comparison of measured and calculated phase behavior for CO_2-C_{16} mixtures at 70°F.
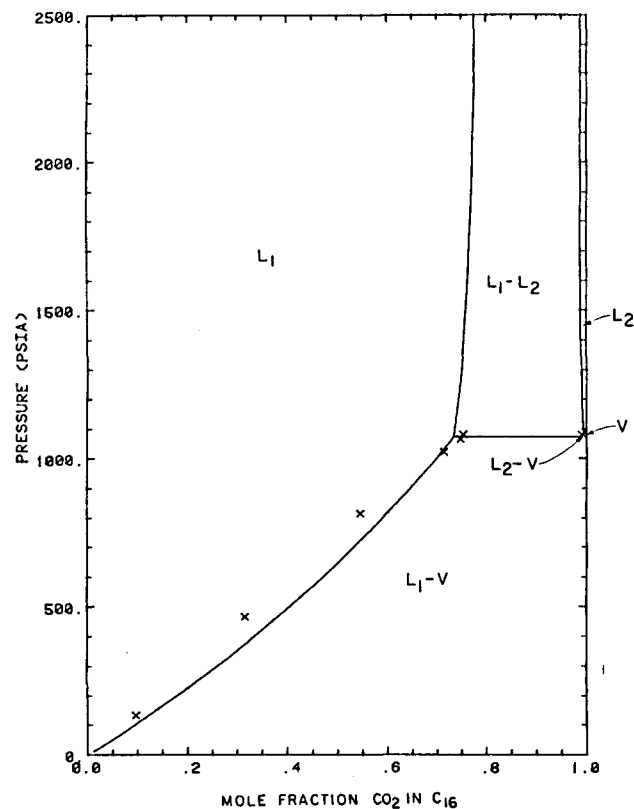
Fig. 2.49 Comparison of measured and calculated phase behavior for CO_2-C_{16} mixtures at 90°F.
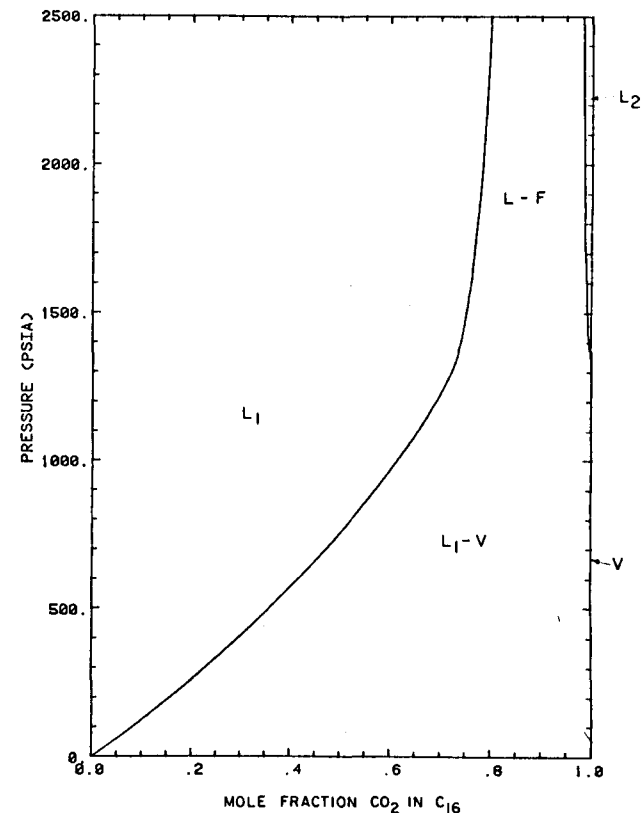
Fig. 2.50 Comparison of measured and calculated phase behavior for CO_2-C_{16} mixtures at 110°F.

64
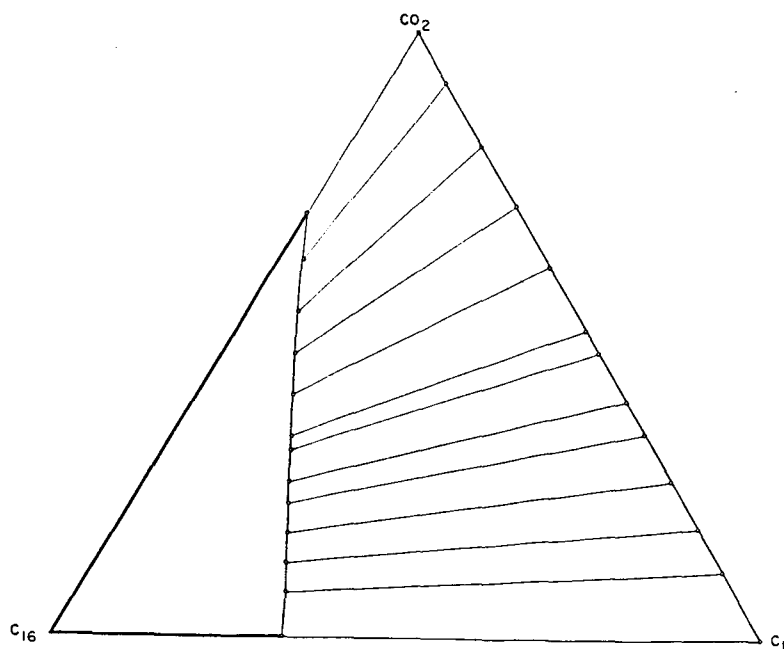
Fig. 2.51   Calculated phase compositions for CO_2-C_1-C_{16} mixtures at 90°F and 1000 psia.
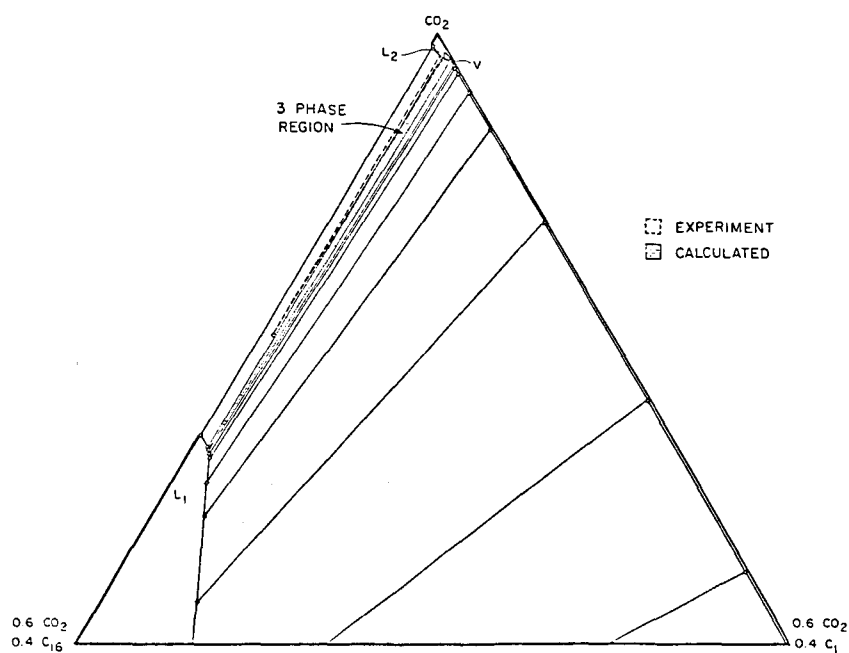
Fig. 2.52   Comparison of measured and calculated L_1, L_2 and V phase compositions for CO_2-C_1-C_{16} mixtures at 90°F and 1110 psia.
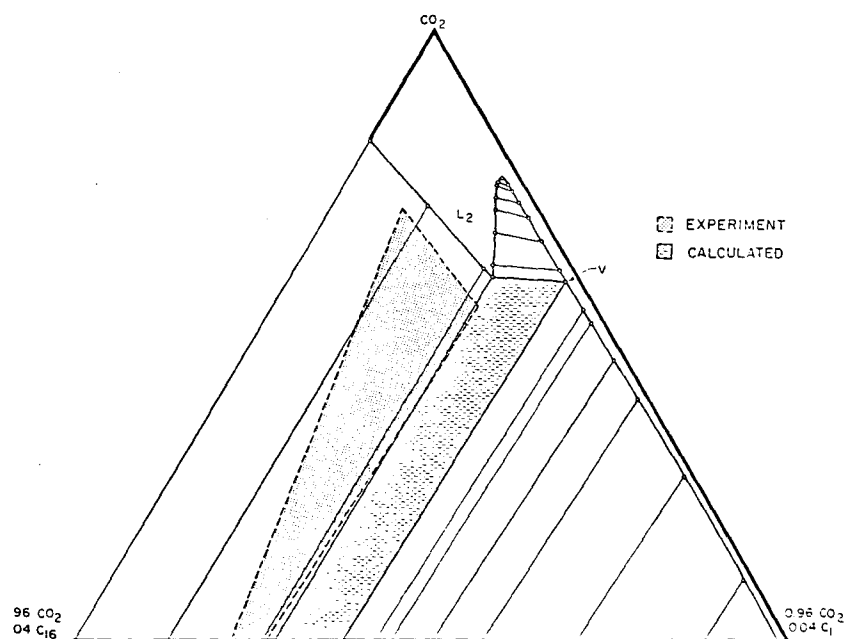
Fig. 2.53   Comparison of measured and calculated L_2 and V phase
            compositions for CO_2-C_1-C_{16} mixtures at 90°F and 1110 psia.
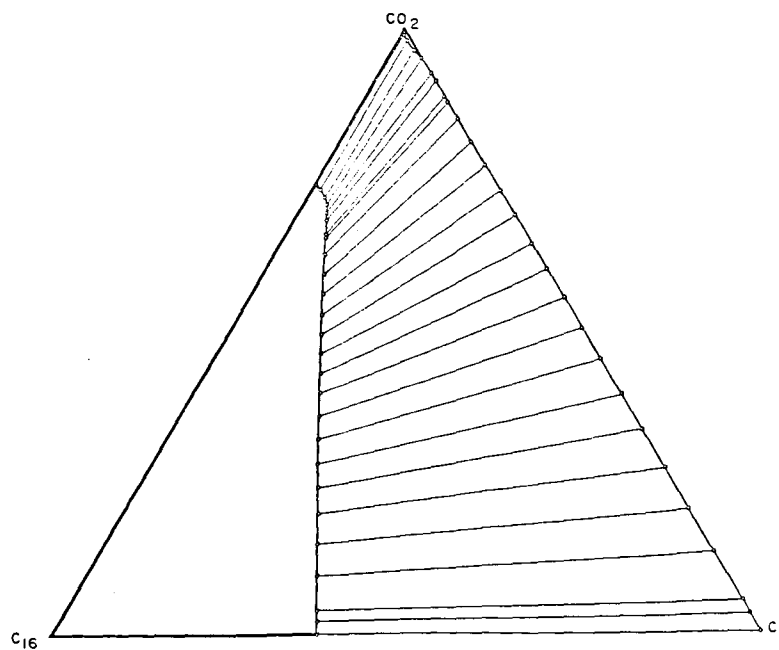
Fig. 2.54   Calculated phase compositions for CO_2-C_1-C_{16} mixtures at 90°F and 1200 psia.

66

Fig. 2.55   Calculated phase compositions for CO_2-C_1-C_{16} mixtures at 90°F and 3000 psia.

Fig. 2.56   Calculated phase compositions for CO_2-C_1-C_{16} mixtures at 90°F and 4000 psia.

identical. The calculated phase diagram at 1200 psia, shown in Fig. 2.54, does not contain a three-phase region. In the experiments described by Orr, Li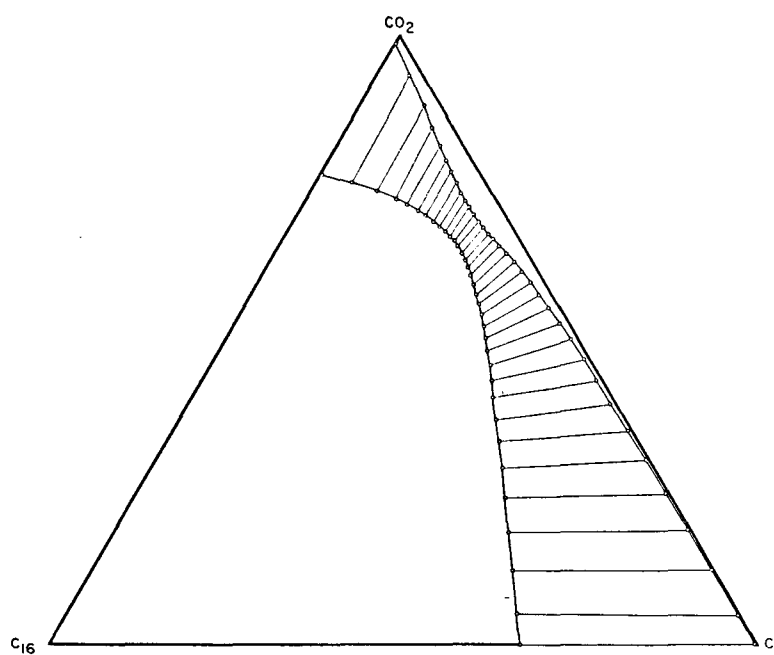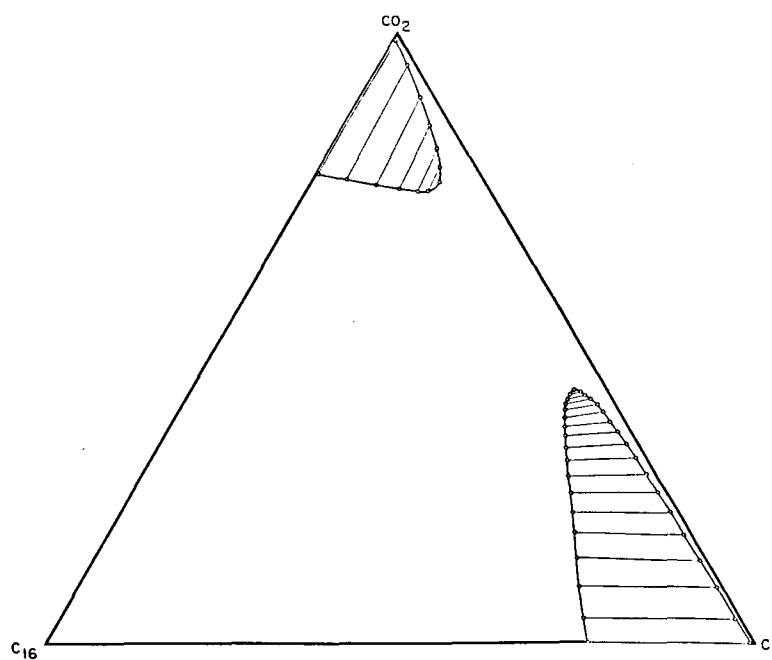en and Pelletier, the three-phase region disappeared at a pressure between about 1150 psia and 1400 psia, but the exact pressure was not determined. The calculated behavior of the system at much higher pressures (3000 and 4000 psia) is shown in Figs. 2.55 and 2.56. Orr, Lien and Pelletier (1981) speculated based on observations of bubble and dew point pressures that the two-phase region must separate into two separate lobes at high pressures. The calculated phase diagram shown in Fig. 2.56 confirms that speculation. Thus, the sequence of phase diagrams shown in Figs. 2.51-2.56 appears to be qualitatively correct and to be in reasonable quantitative agreement where data are available for comparison.

The calculated phase compositions discussed here for well characterized hydrocarbon systems agree well enough with measured values that investigations of the evolution of phase diagrams can be undertaken with some confidence. Much remains to be done in order to show that the phase behavior of CO_2-crude oil systems can be predicted with equal confidence. Nevertheless, the fact that the relatively simple PREOS is as successful as it is for simple hydrocarbon systems which show complex phase behavior suggests that accurate predictions for more complex hydrocarbon mixtures which show similar phase behavior may be within reach.

2.3 Measurement of Viscosity with an Oscillating Quartz Crystal

The continuous multiple contact (CMC) experiment is an efficient technique for measurement of phase compositions and densities. If a measurement of phase viscosities could be added, the experiment would allow simultaneous measurement of fluid properties which would be very useful for estimating the effects of viscous fingering and gravity segregation in a reservoir setting, and for building and testing fluid property correlations. To be suitable for inclusion in the CMC experiment, a viscosity measurement technique should require a small sample volume and should handle conveniently a wide range of viscosities. One technique which appears to meet these requirements uses the damping of the torsional oscillation of a quartz crystal (Mason 1947; Welber 1960; Webeler 1961; De Bock, Grevendonk & Awouters 1967; Collings & McLaughlin 1971; Haynes 1973; Diller 1980; Simon & Schmidt 1983).

A crystal holder similar to that shown in Fig. 2.57 was used to test two mounting schemes. In both, the crystal was capacitively coupled to the driving electric field. Originally, direct plating of platinum electrodes onto the crystal surface was planned, but problems with attaching leads to the crystal led to the arrangement shown in Fig. 2.57. The oscillating electric field is applied to the two pairs of electrodes by an impedance analyzer (Hewlett-Packard HP4192A) which is also used to measure the properties of the crystal. The fluid to be tested resides in the annulus between the electrodes and the crystal. If the crystal is caused to oscillate in a vacuum, it shows a characteristic resonant frequency. In a fluid, the viscous shear at the crystal surface adds damping to the system, which shifts and broadens the
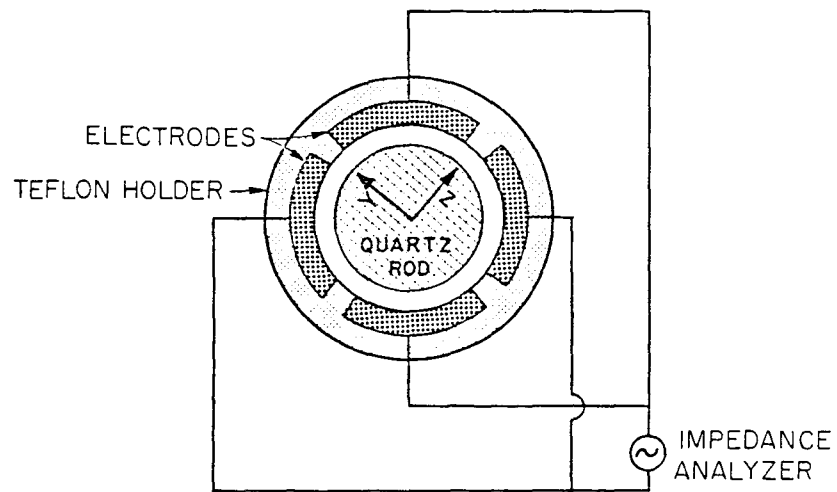
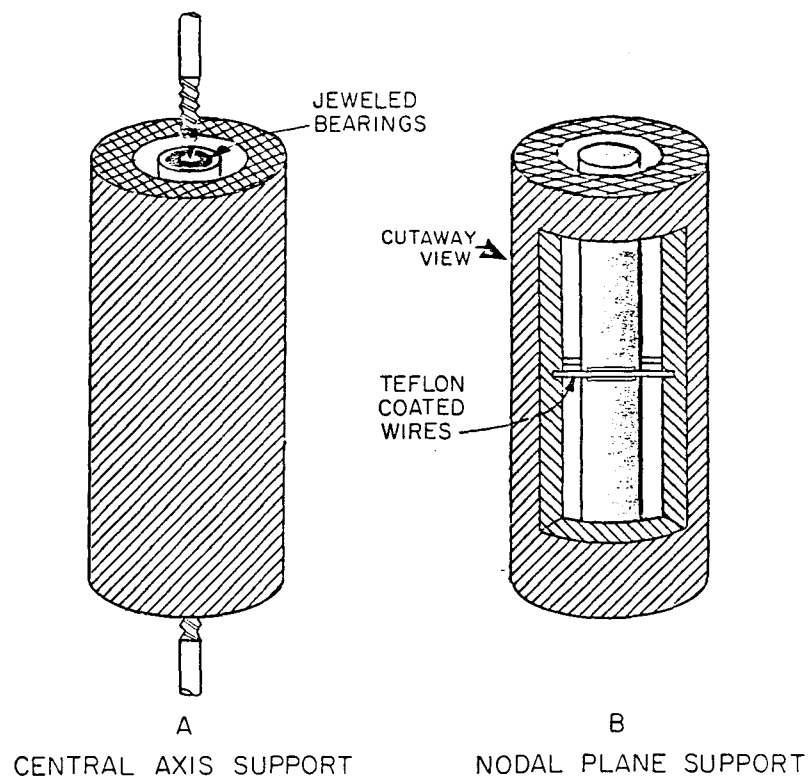Fig. 2.57   Axial view of a cylindrical crystal holder.

A
CENTRAL AXIS SUPPORT

B
NODAL PLANE SUPPORT

Fig. 2.58   Crystal mounting schemes.

69

resonance peak. The change in the band width of the resonance peak can be used to calculate the product of viscosity and density. It is important, therefore, to minimize the damping of the crystal holder itself. If crystal supports make physical contact only at nodes on the cylinder, the damping induced by the mounting is small. In the fundamental torsional node of oscillation, the cylinder axis is a node, as is the plane which bisects the length of the crystal and is perpendicular to the crystal axis. The two mounting schemes, shown in Fig. 2.58, support the crystal at those two nodes.

The first scheme supports the crystal at the axial node. A toroidal jewel bearing was attached with epoxy to each end of the crystal. Small machined metal points were installed in the end plates of the Teflon crystal holder to seat in the toroidal jewels and support the crystal. This method has the advantages of simplicity and mechanical strength, but it proved to have too much damping to allow the crystal to resonate. It also proved difficult to maintain the required orientation of the crystal with respect to the electrodes. Thus, this method appears unlikely to be effective unless a substantial reduction in the damping of the mounting can be achieved.

The second mounting technique is similar to that used by Diller (1980) and Haynes (1973). Two small notches were cut perpendicular to the crystal axis at the crystal midpoint. The crystal was then supported on wires seated in the notches and held in place by tension applied to the wires. This mounting scheme is more susceptible to changes in orientation of the crystal in the electric field, but it has much better damping characteristics than the other method. Sharp resonance peaks were obtained in a vacuum and in several fluids.

For high pressure measurements, the crystal was mounted in a pressure vessel sketched in Fig. 2.59. The sample volume required to fill the cell is about 1.5 cm^3. Fig. 2.60 shows more detail of the mounting arrangement in the high pressure version of the cell. The electrodes were made from 316 stainless steel. Electrode pairs were made in the shape of tuning forks with the crystal supported on fine wires mounted on one of the tuning forks.

In an actual measurement, the width in frequency of the resonance peak is measured. The viscosity of the fluid can then be calculated as (Webeler 1961; Diller 1980)

$$\eta = \frac{\pi f}{\rho} \left(\frac{M}{S} \right)^2 \left(\frac{\Delta f}{f} - \frac{\Delta f_{vac}}{f_{vac}} \right)^2 \qquad (2.2)$$

where

ρ = fluid density (g/cm^3)
η = viscosity (poise)
M = mass of crystal (g)
S = surface area of crystal (cm^2)
f_{vac} = resonant frequency in a vacuum (sec^{-1})
Δf_{vac} = width of resonance peak in a vacuum (sec^{-1})
f = resonant frequency in the fluid (sec^{-1})
Δf = width of resonance peak in the fluid (sec^{-1})

FLUID
INLET

CRYSTAL

FLUID
OUTLET

FITTING
FOR
ELECTRICAL
LEADS

FITTING
FOR
ELECTRICAL
LEADS

Fig. 2.59   High pressure crystal holder.

ELECTRICAL
FEED-THROUGH

ELECTRODE

CRYSTAL

INSULATOR
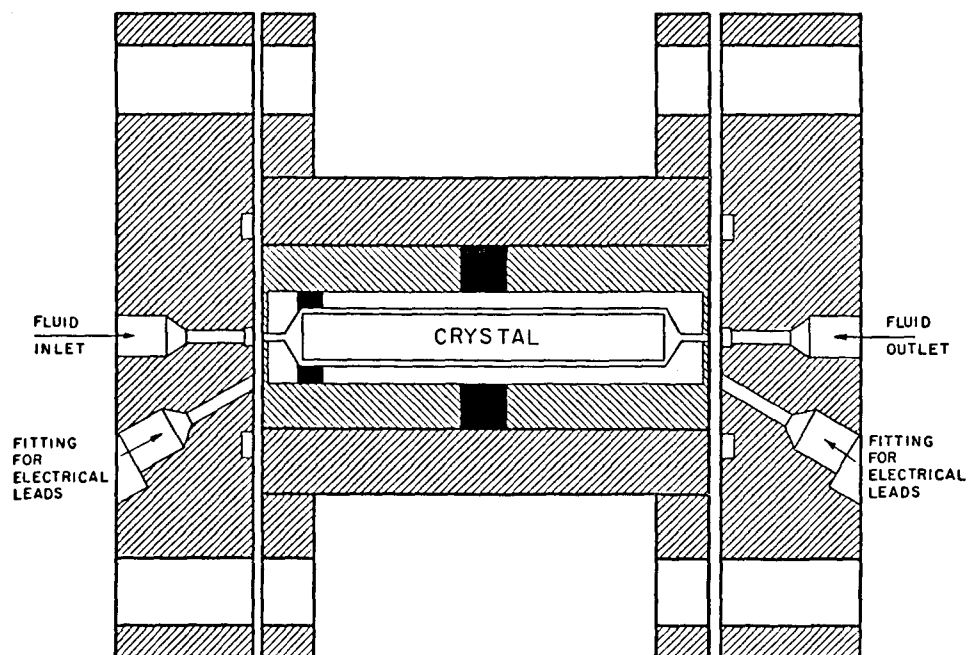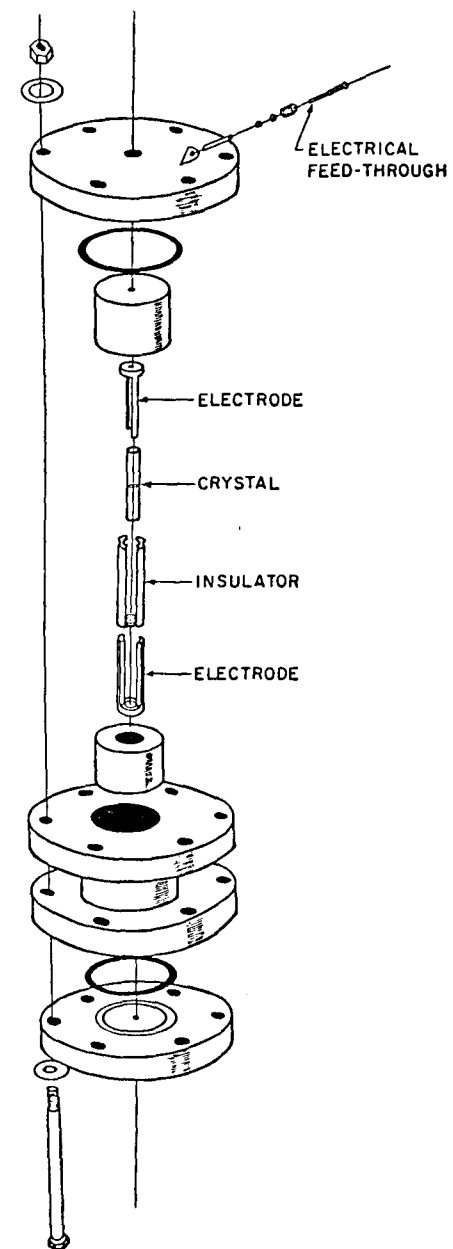
ELECTRODE

Fig. 2.60   Crystal support and electrode
configuration.

Typical results of a measurement of crystal properties in a vacuum are shown in Fig. 2.61. For measurement purposes, the crystal and crystal holder are represented as a conductance and capacitance in parallel. Shown in Fig. 2.61 are the conductance and capacitance of the crystal and holder. The bandwidth Δf is the difference in frequency between the two points at which the conductance is half its maximum value. Bandwidths were measured by the following procedure performed automatically by a microcomputer (Hewlett-Packard HP87):

(1) Determine the resonance frequency, f, as that at which the maximum value of the conductance, G, is obtained.

(2) Measure the conductance at f ± 500 Hz to establish a baseline value, G_o, of the conductance.

(3) Calculate the half conductance $G_{1/2} = 1/2(G - G_o)$.

(4) Determine frequencies, f_1 and f_2, above and below the resonant frequency at which the conductance equals $G_{1/2}$.

Viscosities were then calculated from the bandwidth, crystal properties and fluid density using eq. (2.2). A typical measurement can be completed easily in several minutes. Fig. 2.62 shows results of measurements of crystal properties in heptane at 20°C. Fig. 2.63 shows crystal properties for a more viscous fluid (decane at 25°C). The resonance peak is broader but still easily detectable.

Results of tests to validate the measurement technique over a wide range of viscosities and densities are given in Table 2.16. The same results are plotted in Fig. 2.64. Agreement between measured and reference values was very good for viscosities which vary by three orders of magnitude and viscosity-density products which vary by seven orders of magnitude.

The measurements reported for air indicate the limits of resolution of the measurement for low viscosities and densities. Bandwidths shown differ for the two measurements because different mounts had different vacuum bandwidths. When both viscosity and density are low, the resolution of the frequency generator (0.01 Hz) is not sufficient to resolve the very sharp resonance peaks adequately. Hence, very small differences in measured bandwidths lead to relatively large changes in viscosity, as the differences between maximum and minimum values for air indicate.

For systems of interest in miscible flood applications, however, a resolution of 0.01 Hz should be more than adequate. Fig. 2.65 plots the bandwidth that would be expected as a function of the product of density and viscosity of a fluid. Even for a viscosity of 0.02 cp and a density of 0.1 g/cm^3, the bandwidth would be 1.45 Hz. Thus, a resolution of 0.01 Hz should provide reasonable accuracy for low viscosities as long as the density is not too low and is also known with reasonable accuracy. The density measurement currently being performed in the continuous multiple contact experiment is accurate to about 0.001 g/cm^3. Thus, high precision viscosity measurements for gases appear to be possible with the existing instrumentation.
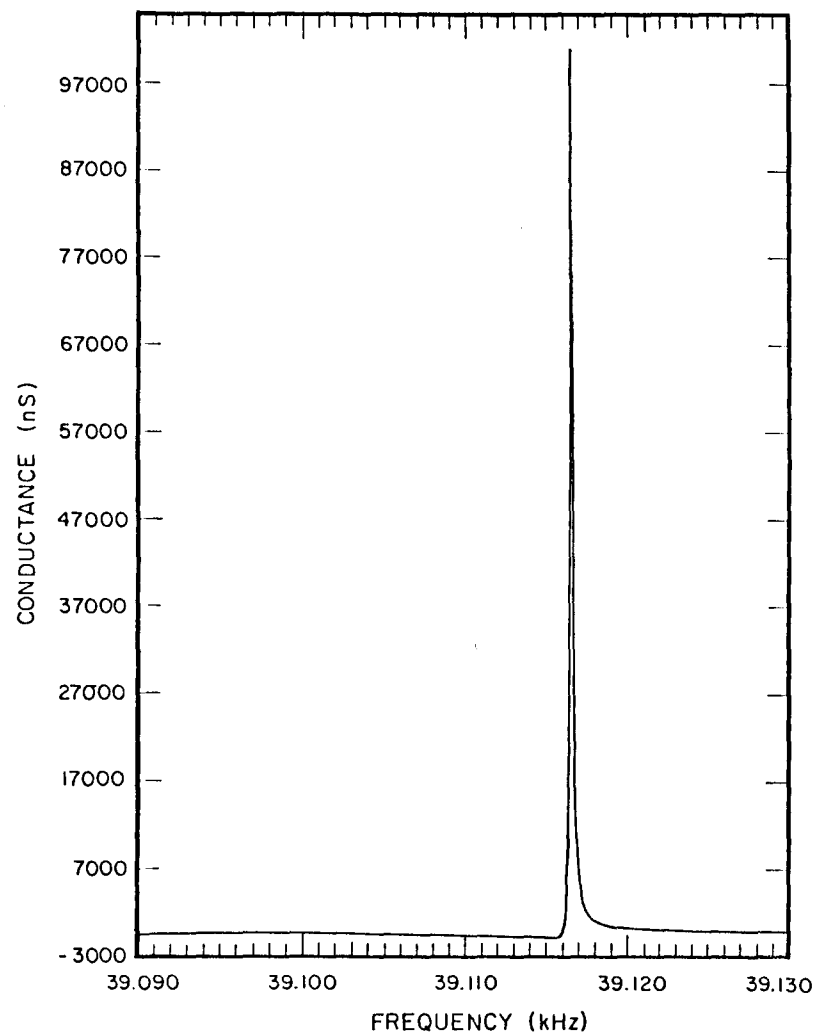
a. Conductance
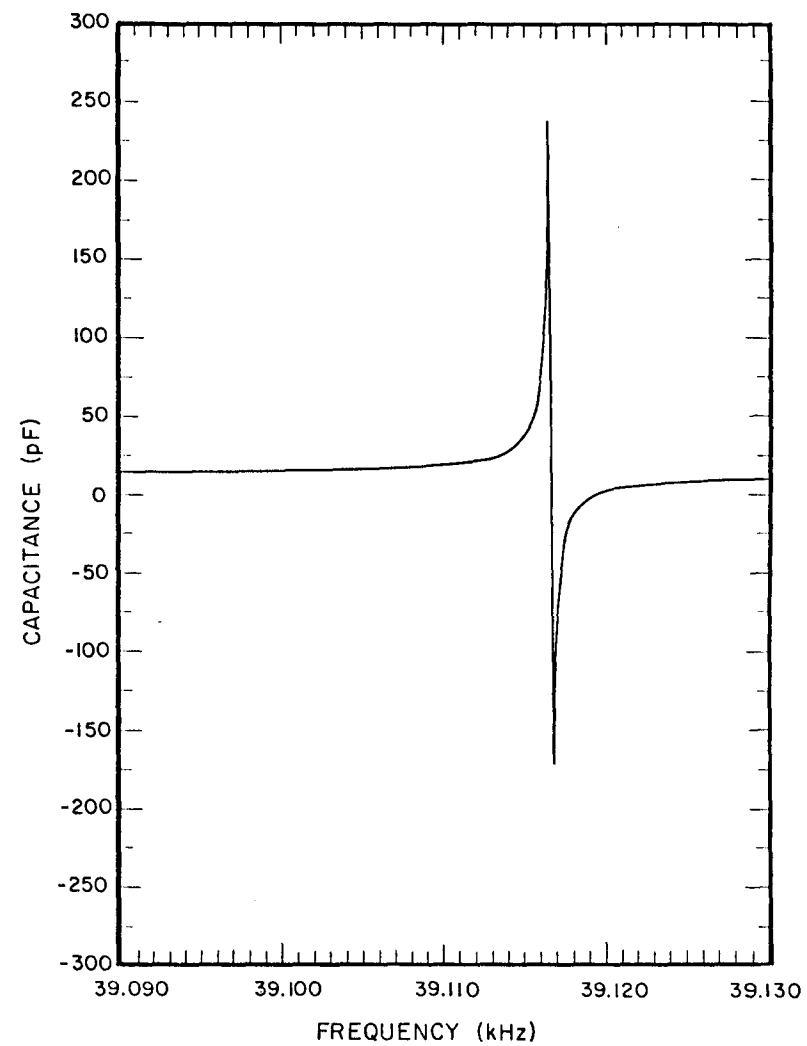
b. Capacitance

Fig. 2.61 Crystal response in a vacuum.
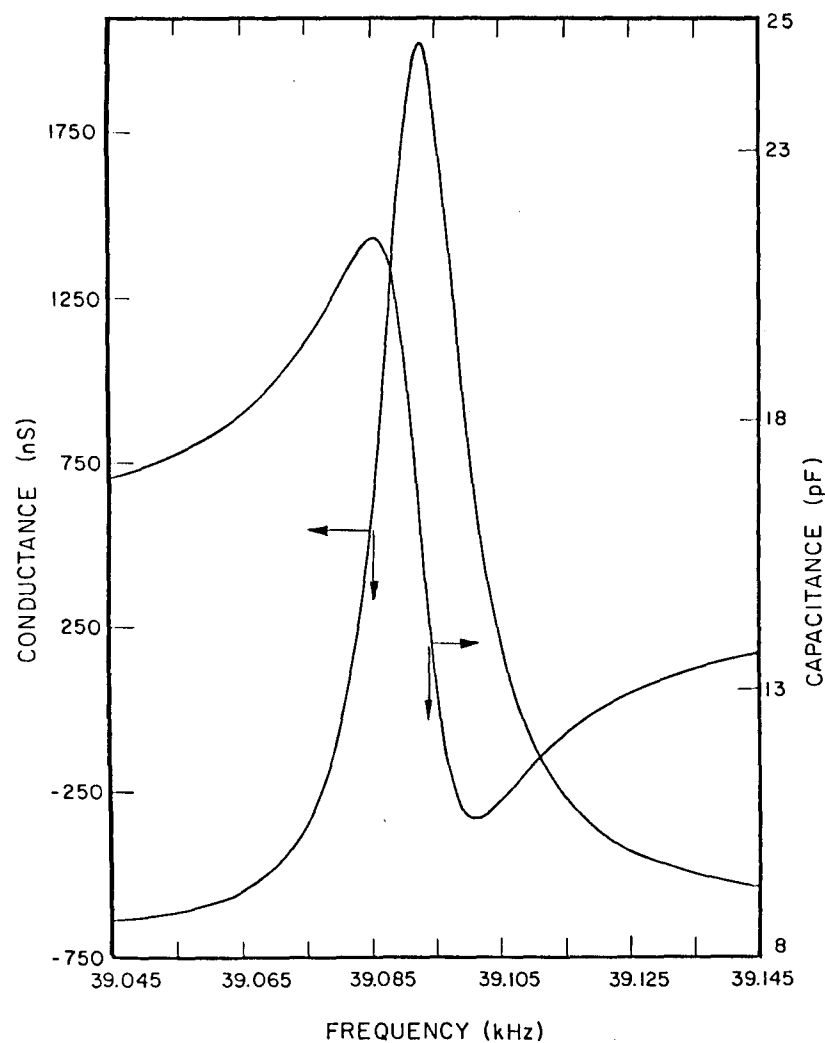
Fig. 2.62   Capacitance and conductance of the
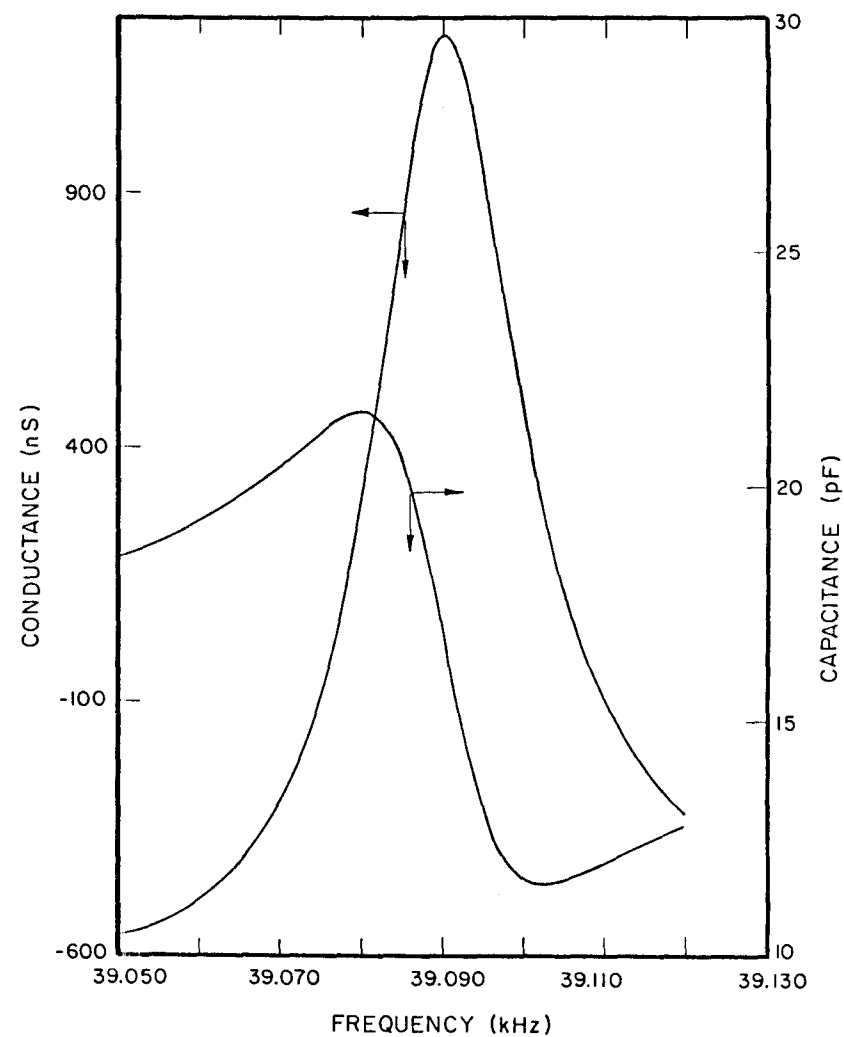   quartz crystal in heptane at 20°C.

Fig. 2.63   Capacitance and conductance of the
             quartz crystal in decane at 25°C.

74

Table 2.16   Results of Viscosity Measurements

Run	Fluid	Bandwidth (Hz)	Density (g/cm^3)	Measured Viscosity (Crystal) (cp)	Reference Viscosity (cp)	Difference (%)
1	Air (28.9°C, 649 Torr)	0.32	0.001	0.0237	0.0185*	28.1
2	Air (20°C, 621 Torr)	0.2125 (Ave.)	0.001	0.0183 (Ave.)	0.0185*	1.1
		0.215 (Max.)		0.0215 (Max.)		16.2
		0.20 (Min.)		0.0165 (Min.)		-10.8
3	CO_2 (30.4°C, 904 psia)	1.86	0.1827	0.0193	0.0194*	-0.5
4	CO_2 (31.4°C, 1296 psia)	6.425	0.7489	0.0634	0.0646*	-1.8
5	CO_2 (31.4°C, 1361 psia)	6.577	0.7620	0.0681	0.0667*	2.1
6	n-Heptane (20°C)	15.30	0.6838	0.414	0.409	1.2
7	i-Octane (25°C)	16.62	0.6880	0.488	0.479	1.9
8	n-Decane (20°C)	23.54	0.7301	0.928	0.928	0
9	n-Decane (20°C)	23.43	0.7301	0.920	0.928	-0.9
10	n-Decane (25°C)	22.50	0.7251	0.853	0.860	-0.8
11	Soltrol 130 (20°C)	30.41	0.7559	1.50	1.48**	1.4
12	n-Hexadecane (20°C)	46.69	0.7733	3.47	3.34	3.9
13	Wasson Crude Oil (32°C)	67.42	0.86	6.53	6.23**	4.8

* Calculated with TRAPP (Ely and Hanley 1981). Other reference viscosity data obtained from CRC Handbook (1968), Lange's Handbook (1979).

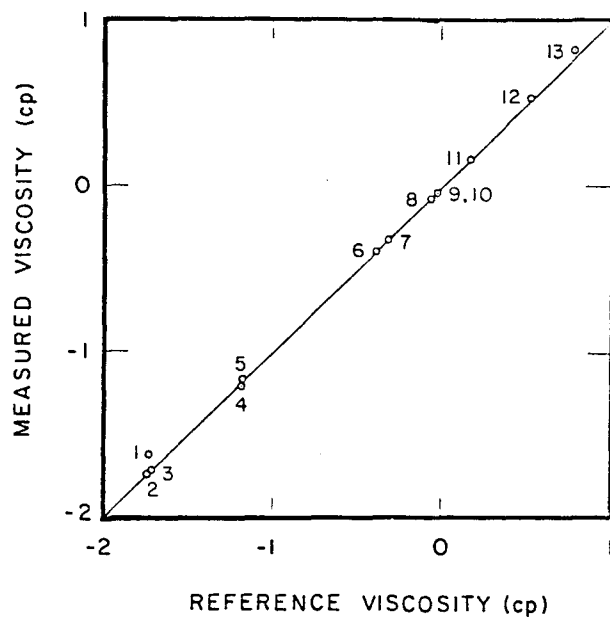** Measured with an Ostwald viscometer tube.

Fig. 2.64   Comparison of fluid viscosities measured with an oscillating quartz crystal with literature values.
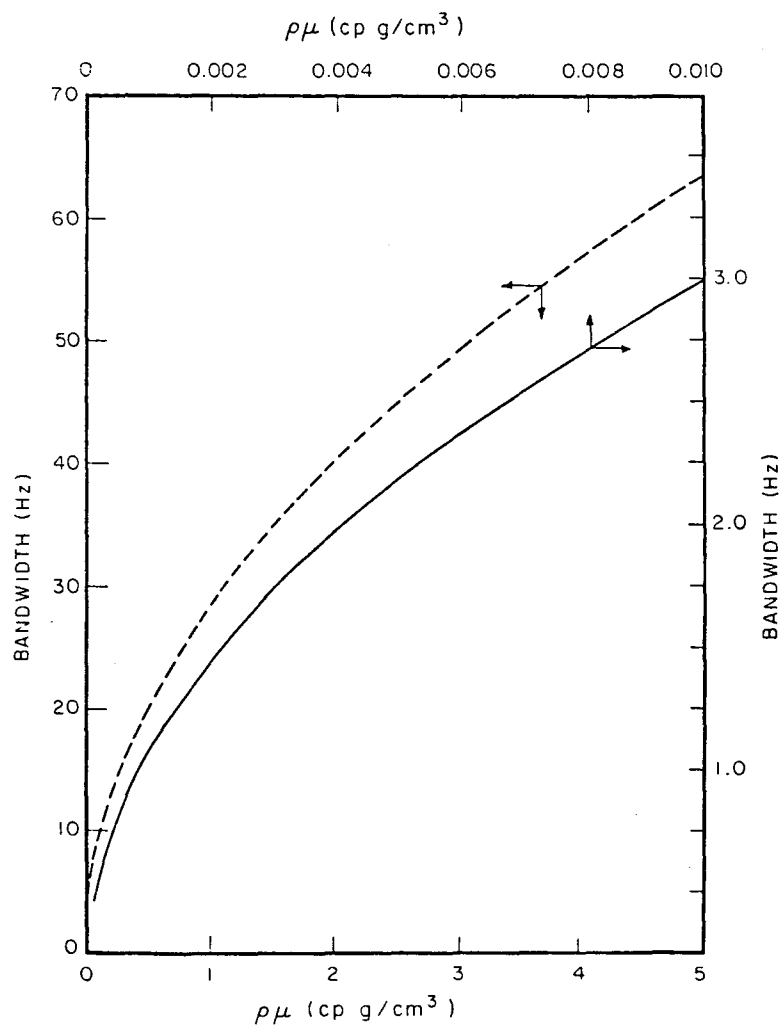

Fig. 2.65   Expected bandwidth as a function of the product of density and viscosity.

2.4 Summary and Conclusions

In this chapter, results of an extensive set of experiments to investigate the phase behavior and fluid properties of CO_2-hydrocarbon mixtures are presented. Analysis of the phase diagrams obtained in single-contact, static equilibrium PVT experiments was used to construct simple techniques, based on the idea that density of the CO_2-rich phase strongly affects displacement performance, for estimating the effects of changing system temperature or injected fluid composition. Continuous multiple contact measurements of phase compositions for CO_2-crude oil systems and CO_2-synthetic oil systems were used to examine the role of oil composition (molecular weight distribution and molecular type) in the development of miscibility. Measured phase compositions for quaternary and ternary systems (CO_2-C_1-C_4-C_{10} and CO_2-C_1-C_{16}) were used to test the performance of the Peng-Robinson equation of state for systems showing the complex phase behavior of some CO_2-hydrocarbon mixtures. Finally, the development and testing of a viscometer based on an oscillating quartz crystal was described. The investigations outlined here lead to the following conclusions:

(1) The maximum temperature at which L_1-L_2-V phase separations occur depends on the composition of the oil. Addition of solution gas to a dead oil reduces the maximum temperature for L_1-L_2-V formation. Addition of contaminants such as N_2 to the CO_2, which reduces the density of the CO_2-rich phase, also reduces the maximum temperature.

(2) For dead oils, the L_1-L_2-V region occurs at pressures close to the vapor pressure of CO_2, extrapolated if the temperature is greater than the critical temperature of CO_2.

(3) For live oils, the lower pressure limit of the L_1-L_2-V region is the extrapolated vapor pressure of CO_2. When the CO_2 is contaminated by N_2, the lower pressure limit of the L_1-L_2-V region can be estimated as the pressure required to compress the CO_2-N_2 mixture to the critical density of CO_2.

(4) The extrapolated vapor pressure is a reasonable estimate of the pressure required to make a CO_2-rich phase dense and relatively incompressible. Such a phase should extract hydrocarbons efficiently. Thus, the extrapolated vapor pressure plus a suitable safety margin can be used as an estimate of the MMP.

(5) If some slim tube data are available, then the CO_2 density required for efficient displacement can be estimated. The pressure required to produce the same density at a different temperature or with contaminants present in the CO_2 is an estimate of the MMP at the new conditions. That pressure can be calculated with a suitable equation of state.

(6) The addition of about 15 wt. % (22 mol %) of a mixture of aromatic hydrocarbons to a paraffinic crude oil had little effect on the partitioning of hydrocarbon components when CO_2 was mixed with the

new oil. The aromatic components were extracted less efficiently than constituents of the crude oil having the same number of carbon atoms. The presence of the aromatic hydrocarbons had very little effect on the total amount of hydrocarbons extracted into the CO_2-rich phase.

(7) Measurements of partition coefficients for synthetic oils containing normal alkanes, branched alkanes, aromatics and naphthenes in liquid-liquid mixtures with CO_2 indicate that for oils having approximately the same distribution of molecular weights, the sequence of MMPs (lowest to highest) should be: branched alkanes, normal alkanes, aromatics and naphthenes. Additional experiments are needed to examine the effects of paraffinic side chains on extraction of naphthenic and aromatic hydrocarbons.

(8) Comparison of measurements of phase compositions and densities for binary, ternary and quaternary mixtures of CO_2, C_1, C_4 and C_{10} with available static equilibrium data confirm that the continuous multiple contact experiment yields measurements of reasonable accuracy.

(9) Phase compositions for CO_2-C_1-C_4-C_{10} mixtures calculated with the Peng-Robinson equation of state agreed well with measured values. Vapor phase densities agreed closely with measured values, but liquid phase densities were less accurate. Calculated phase behavior for the CO_2-C_1-C_{16} system showed good qualitative and quantitative agreement with measured phase behavior, even for liquid-liquid and liquid-liquid-vapor systems. Agreement between calculation and experiment was good enough to suggest that the equation of state can be used with confidence to interpolate existing experimental data and to investigate evolution of phase diagrams with changes in temperature and pressure.

(10) Viscosities of high pressure fluids can be measured accurately with a viscometer based on an oscillating quartz crystal. With such a device mounted in a flow cell, simultaneous measurements of compositions, densities and viscosities for two phases in equilibrium should be possible in the continuous multiple contact apparatus.

3. FLOW VISUALIZATION EXPERIMENTS

The phase compositions which occur in any real displacement are the result of mixing which takes place when oil and CO_2, and the phases which form as they mix, flow in a porous medium. In §4, we consider effects of reservoir rock pore structure and the distribution of phases within the pore space on the mixing of flowing fluids. In the experiments described in §4, simple fluids of matched density and viscosity were used in an attempt to eliminate the complications of phase behavior and resulting fluid property variations so that the displacement experiments in complex pore structures could be interpreted with less ambiguity. In this section, we consider another limiting case, the flow of complex fluids, CO_2, oil and water, in very simple porous media, two-dimensional pore networks etched in glass. Results of both secondary and tertiary CO_2 floods are compared with first contact miscible floods and with immiscible nitrogen (N_2) floods in the same models. Also described are experiments in which oil is recovered from dead-end pores. Those experiments show clearly that CO_2 can diffuse through water to reach trapped oil. Based on those observations, a new experiment designed to provide quantitative measurements of diffusion coefficients in oil and water at high pressure is described (§3.3). Much of the material in §3 is also available in a paper by Campbell and Orr (1983). Additional details of the experiments are reported by Campbell (1983a).

The displacement experiments described here are not without limitations, and hence, they must be interpreted with care. The pore networks do not, of course, represent all the complexity of reservoir rocks. Pores in reservoir rocks are smaller, have more widely varying shapes, and are connected in three dimensions. Nevertheless, the physical causes of mixing of oil, water and CO_2, convection, diffusion, dispersion, and viscous instabilities still operate in the model displacements, though the time and space scales of the individual contributions differ from those in rocks. Thus, the results presented illustrate the effects of physical mechanisms which must operate in displacements in reservoir rocks but do not give quantitative information about the relationships between the mechanisms.

The only previous flow visualization study of CO_2-crude oil displacements is that of Wang (1980, 1982). His experiments were performed in a long (1.5m), relatively narrow (1.3 cm) pack of glass beads 0.8 to 1.0 mm in diameter. The pack (2.2 mm thick) contained one or two layers of beads and was oriented so that the long direction was horizontal or slightly dipping. The thin rectangular space in which flow was observed was set on edge. The displacements described by Wang differed substantially from those presented here. Despite the fact that Wang's displacements were run at high velocities (101 ft/day, 3.6 x 10^{-2} cm/sec), the loose packing, large beads, and pack orientation produced displacements dominated by gravity. In the study reported here, the pore networks were horizontal so that gravity effects were eliminated. Flow velocities were nearly an order of magnitude lower (15 ft/day, 5.3 x 10^{-3} cm/sec), and the pore networks were much smaller, with a typical volume of about 0.25 cm^3 vs. 22 cm^3 for Wang's beadpack. Thus, the observations reported here were aimed at events at the pore level rather than at the development and movements of banks of oil, water and CO_2.

3.1 Experimental Apparatus

Fig. 3.1 shows pore network patterns used in this study. Mirror images of each pattern were etched in two glass plates using a photofabrication technique similar to that used in the production of printed circuits. Details of the fabrication process have been reported by Chatzis (1982), Chatzis, Morrow and Lim (1983), and Campbell (1983a). The mirror images were aligned and heated to fuse the glass plates. Fig. 3.2 shows a cross section of a typical pore from micromodel 3. As the plates are fused, the pores shrink slightly, and pore surfaces and corners are smoothed. Large pores, such as the one shown in Fig. 3.2, take on an elliptical cross section. Smaller pores become more circular. Approximate dimensions for the pore throats and bodies for each model are given in Table 3.1.

For high pressure displacements, the micromodels were placed in the apparatus shown in Fig. 3.3, details of which are given by Campbell (1983b). Low pressure displacements were performed in a similar but slightly simpler version of the apparatus. In the high pressure displacements, the glass models were placed in a pressure cell with polycarbonate windows. The cell was filled with glycerine which applied containment pressure to the model. The glycerine was pressurized by the injected CO_2, so there was essentially no pressure difference between the interior of the glass model and the glycerine. After the model had been filled with oil or oil and water, the pressure in the CO_2 pump was set slightly higher than the pressure in the nitrogen vessel, and flow was started through the bypass line. Because the pressure drop needed to move fluid through the model was very small, careful balancing of the CO_2 and N_2 pressures was required to prevent rapid flow from one vessel to the other. When flow through the bypass line was stable, the bypass valve (V_1 in Fig. 3.3) was closed, the cell inlet valve (V_2) opened, and CO_2 injected into the model. The displacements were observed on a color television monitor and were recorded on videotape.

Properties of the fluids used in the displacement experiments are summarized in Table 3.2. All of the displacements were performed at 25°C. High pressure displacements were performed at 8.3 MPa (1200 psia). At those conditions, the CO_2 was a liquid which was first contact miscible with Soltrol 130, a mixture of C_9-C_{13} branched alkanes. The displacement pressure was above the minimum miscibility pressure for Maljamar crude oil at 25°C (77°F). As Fig. 2.5 shows, the vapor pressure of CO_2 at that temperature is about 930 psia (6.4 MPa). At higher pressures, liquid CO_2 is dense enough to produce high local displacement efficiency (see §2.1 and Orr & Jensen 1984). Results of extensive phase behavior experiments for mixtures of CO_2 with Maljamar crude oil are available (Orr, Silva & Lien 1983; Orr, Yu & Lien 1981; Orr & Taber 1981; Orr & Taber 1982). Low pressure displacements were performed at 5.52 MPa (800 psia) and 25°C. At those conditions, both the CO_2 and the N_2 had low densities and were immiscible with Maljamar crude oil.

All displacements were performed at a nominal rate of 0.05 PV per minute (0.66 to 1.05 cm^3/hr). In the CO_2 displacements, however, there was considerable uncertainty in the actual displacement rate. For example, at 8.3 MPa, the density of CO_2 is sensitive enough to temperature change that small
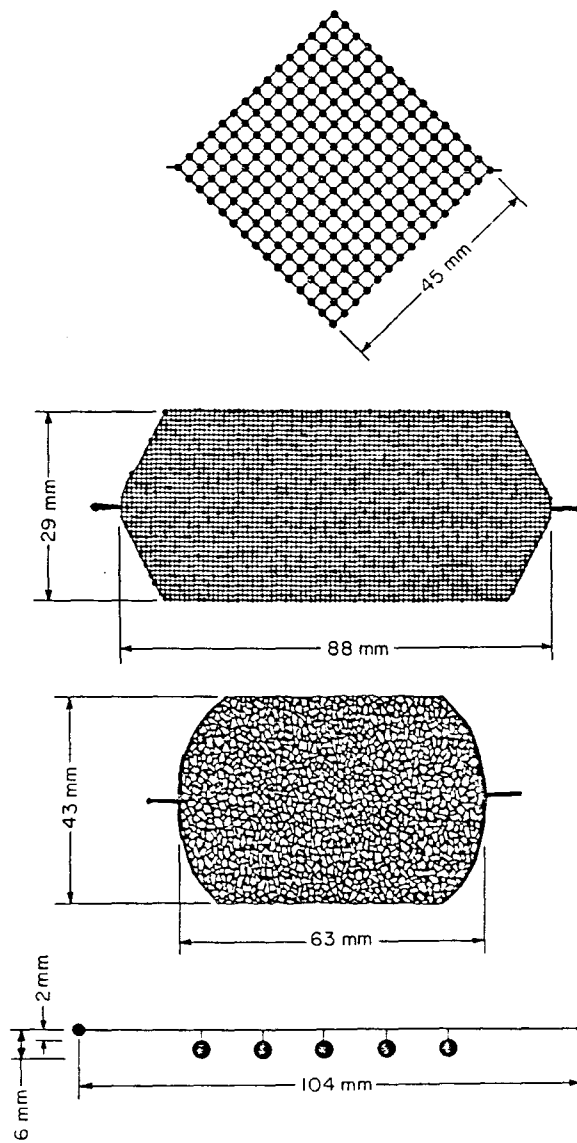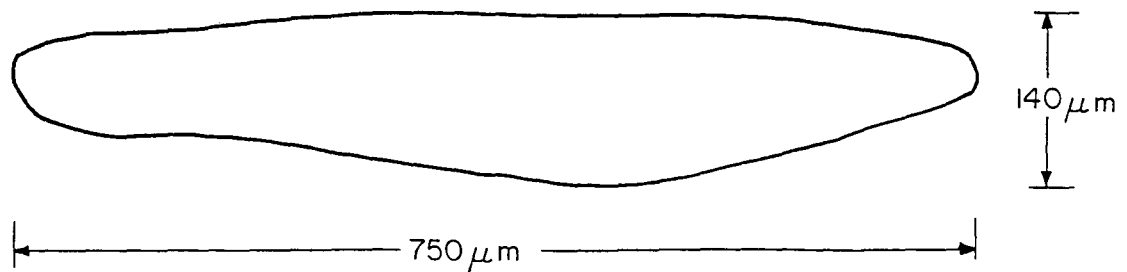
Fig. 3.1   Pore network patterns for glass micromodels.

Fig. 3.2   Cross section of a pore after fusion of etched glass plates.

Table 3.1   Properties of Pore Networks

Model	Pore Volume	Pore Throat Diameter (mm)	Pore Body Diameter (mm)	Pore Thickness* (mm)
1	0.22	0.5	1.9	0.2
2	0.35	0.2	0.7, 0.9, 1.1	0.2
3	0.24	0.4-1.0	1.0-1.3	0.3
4		0.4	4.0	0.3

*Measured before fusing. After fusing, pore thicknesses were somewhat smaller.

Table 3.2   Properties of Fluids Used in Displacement Experiments

Fluid	Density (g/cm^3)	Viscosity (mPa·s)
CO_2 (8.3 MPa, 25°C)	0.779	0.067
CO_2 (5.5 MPa, 25°C)	0.156	0.018
N_2 (5.5 MPa, 25°C)	0.063	0.019
Maljamar Crude Oil	0.813	3.3
Soltrol^{TM} + Red Dye*	0.748	1.45
Soltrol^{TM} + Blue Dye**	0.748	1.45
Water	0.997	0.89

 *Oil Red O No. 0-0625, Sigma Chemical Co.

**Oil Blue N No. 0-8376, Sigma Chemical Co.

^{TM} Soltrol is a registered trademark, Phillips Petroleum Co.